

Revealing the Substitution of Zn²⁺ on Nano-Structural, Magneto-Electrical, Antibacterial and Antifungal Attributes of Nickel Oxide Nanoparticles via Sol-Gel Strategy

Aslinjensipriya A

Sylvia Reena R

Ragu R (✉ ragu.r31@gmail.com)

<https://orcid.org/0000-0002-1809-6763>

Grace Infantiya S

Jerome Das S

Research Article

Keywords: NiO nanoparticles, Wemple-DiDomenico model, Urbach energy, BET, magnetic property, antibacterial, and antifungal activity

Posted Date: March 15th, 2022

DOI: <https://doi.org/10.21203/rs.3.rs-1440199/v1>

License:   This work is licensed under a Creative Commons Attribution 4.0 International License.

[Read Full License](#)

Revealing the substitution of Zn²⁺ on nano-structural, magneto-electrical, antibacterial and antifungal attributes of nickel oxide nanoparticles via sol-gel strategy

A. Aslinjensipriya^a, R. Sylvia Reena^a, R. Ragu^{a*}, S. Grace Infantiya^a, S. Jerome Das^a

^aDepartment of Physics, Loyola College (Autonomous), Affiliated to University of Madras, Chennai 600 034, India

*Corresponding author: ragu.r31@gmail.com

Abstract

Transition metal oxides have gathered momentum among the scientific community on account of their peculiar procession in physico-chemical, opto-electronic, magnetic, electrochemical, and biological attributes resulting from anisotropic charge distribution of partly filled d-orbitals, non-stoichiometric behaviour, and diverse oxidation states of the cations. The current work emphasize on the systematic synthesis and characterization of pure and zinc (Zn) incorporated nickel oxide (NiO) nanoparticles in varying concentrations Zn_xNi_{1-x}O (x=0, 0.1, 0.2, and 0.3) via a scalable sol-gel approach assisting citric acid (C₆H₈O₇) as a congealing factor. A series of extensive analyses were executed to investigate the structural, opto-electrical, and magnetic characteristics of prepared nanoparticles. X-Ray Diffraction (XRD) studies confirmed the face-centered cubic structure of as-synthesized samples and the corresponding crystallite size is found to decrease with an increasing dopant concentration as estimated from the Scherrer method. Scanning electron microscopy studies portrayed the spherical structure and porous nature of NiO nanoparticles. Particle size calculated from SEM shows the decreasing trend with dopant discrepancy which is in accordance with crystallite size measured from XRD results. Energy Dispersive X-ray (EDX) spectra revealed the presence of estimated molecular assembly in synthesized samples. The cubic configuration and the presence of functional groups existing in synthesized nanoparticles were endorsed from Fourier Transform Infra-Red (FTIR) spectra. The optical absorption spectrum examined from UltraViolet-visible (UV-vis) spectroscopy evaluates the energy bandgap and it is noticed to increase from 2.48 to 2.87 eV affirming the Burstein Moss shift. The energy dispersion of optical parameters plays a crucial contribution in optical materials pursuant to its prominence in optical communications and in fabricating novel devices for spectral dispersion. Optical and energy dispersion parameters evaluated from Wemple-DiDomenico (WDD) model and non-linear optical parameters were deliberated from optical studies. Urbach energy and another pivotal optical criterion highly correlated with the bandgap energy anchored in the fabrication of optoelectronic devices were assessed. The electrical characteristics such as dielectric constant, loss, and conductivity exhibited by pure and Zn doped nickel oxide nanoparticles were reported. Molecular electronic polarizability assessed through elementary solid-state parameters is in better concurrence with diverse relations like Clausius-Mossotti, Lorentz-Lorent, bulk modulus, optical electronegativity, energy band gap. The pore size distribution of substance matrix and the associated surface area were elucidated from Brunauer-Emmett-Teller (BET) analysis. Dispersive magnetic properties and two pivotal parameters were derived from the Law of Approach to Saturation (LAS) operandi. Further, microbial cell mechanism was illustrated through nano-architecture design, and the antibacterial and antifungal activity encountered by undoped and zinc doped NiO

nanoparticles against different microbial strains were deeply discussed for pilot production of antimicrobial agents.

Keywords: NiO nanoparticles, Wemple-DiDomenico model, Urbach energy, BET, magnetic property, antibacterial, and antifungal activity

1. Introduction

In the recent decade, worldwide agricultural sectors are frequently facing extreme challenges due to abrupt climate variants and harmful microbes. Fungi affect around 70% of crop plant diseases in pulses, fibers, fruits, etc. Traditional crop preservation or plant disease control schemes commonly involve overdosing of fungicides in plants [1-2]. Soil contamination is another secondary detrimental issue arising due to insecticides administration. In addition, infectious diseases mediated by pathogenic microorganisms frequently threaten and pose a serious hazard to human health. The inappropriate utilization of antibiotics, lack of competencies, and scientific tools to generate such drugs had resulted in the emergence of mutations and generations of micro-organisms that are immune to such medications. Recently, antibiotic resistance has been experiencing exponential growth, necessitating the development of novel antibacterial systems as a core therapeutic requirement for treating wounds. The mass development of antimicrobial agents that can either inhibit or annihilate the growth and reproduction of deleterious microbes such as bacteria and fungi is one of the inquest domain that coerces a continuous research effort among the research commune [3-4]. Modern nanotechnology has aided in the progress of crop preservation policies and ensuring integrality in agriculture to achieve food security by creating a revolution in the field of agricultural systems viz., improving farming procedures, and minimizing the excessive use of non-degradable pesticides by synthesizing bio-compatible and eco-friendly nanoparticles. Aside from the environmental concern, nanotechnology might bring benefits for agriculture particularly for seed priming [5]. A confluence between nano-engineering and bio-science can potentially resolve a slew of biomedical complications by optimal synthesis of nanomaterials [6-7]. Various nanomaterials, notably metal oxide nanoparticles (NPs), carbon nanostructures, and other non-metallic nanoscale structures, have demonstrated phenomenal antibacterial, antifungal and anticancer activities by virtue of their dimensions in nanometers, distinctive chemico-physical, magneto-electrical, and high specific surface area [8]. Particularly, semiconductor metal-oxides have earned excessive emphasis in environmental remediation attributable to their electronic structure, superior potential to absorb light and unique charge transport capabilities. A critical assessment of the current condition of metal and metal-oxide nanomaterial research upgrades our understanding to strife antibiotic resistance and proposes alternatives to antibiotics in the fight against bacterial illnesses [9]. Nickel oxide (NiO) being the chemically stable material among the transition metal oxide family exhibiting p-type semiconducting behaviour with a widespread energy band gap of 3.5-4 eV [10] with intriguing applications in the field of opto-electronics, spintronics, optical fibers, lithium (Li)-ion batteries, assembly of proficient solar and fuel cells, super-capacitors, flat displays, gas sensors, photodiodes, photo-catalyst in the deterioration of synthetic and organic dyes, designing antiferromagnetic layers, and in biomedical disciplines by adeptly manipulating the

functional dynamics of synthesized nanomaterials [11-15]. Scientists confront several constraints in modifying the synthesis technique and circumstances to execute the peak performance in nanomaterials for varied applications. Doping is the prime procedure for competently controlling the facial characteristics of nanoscale-structured semiconductors and in acquiring technologically important material by creating an island of charge carriers, resulting in significant variations in their existing opto-electrical, magnetic and biological traits [16-21].

In this work, nickel atoms were doped with varying amounts of zinc atoms, and the related change in existing opto-electrical, magnetic, antimicrobial activity of NiO nanoparticles was investigated. Bulk NiO is naturally antiferromagnetic with a Neel temperature (523 K) and doping a non-magnetic semiconductor (Zn) with nickel oxide nanoparticles results in the production of Dilute Magnetic Semiconductors (DMS), which exhibit ferromagnetic activity at room temperature. The distinguishing characteristics of DMS is the strong spin-spin swap interaction between the electrons in the empty band of minimum and/or maximum energy and the localized magnetic moments of the ions. These form of interactions have a significant impact on the electromagnetic characteristics of the nanomaterial and in turn, the spin-based multifunctional devices have assorted applications in the scope of spin-polarized light emitting diodes (LEDs), sensors, spintronics, photovoltaic, magneto-optoelectronics, high-density information storage, quantum computing, field-effect transistors, etc. credited to its faster data processing speed, non-volatility and greater integration densities, etc [22-24]. ZnO being the n-type semiconductor with bandgap energy of ~3.32 eV and exciton binding energy 60 MeV, is reported as a biocompatible compound viz., extreme resistant towards microbes, heat resistant, reduced toxicity material with a wide range of applications including transparent electronics, piezoelectric, chemical and biological sensors, as an antimicrobial agent and in catalytic processes. Zn^{2+} has a $3d^{10}$ and Ni^{2+} possesses $3d^8$ electronic configuration at the outermost shells, substituting Zn^{2+} for Ni^{2+} is expected to impact the electrical and magnetic characteristics of NiO [25]. Several researchers worked on ZnO material doped with other metals majorly focussing on bio-medical applications due to their exceptional properties such as antibacterial, antifungal, antioxidant, and anticancer activities. Bhosale et al synthesized zinc oxide nanoparticles via co-precipitation technique assisting sodium dodecyl sulphate as a capping agent and deeply discussed the photo-degradation of methyl orange and its antibacterial activity [26]. Perveen et al compared the antimicrobial response of ZnO nanoparticles prepared through both green and sol-gel methods of approach [27]. ZnO synthesized in the nanocomposite network, NiO.CeO₂.ZnO via co-precipitation method fetches its application in the antibacterial assay as reported by Abdus et al [28]. Ferin et al synthesized pure and iron (Fe) doped ZnO nanoparticles in the absence of reducing agents chemically and investigated the antifungal response [29].

The predominant generation of hydroxyl ($\cdot OH$) and superoxide free radicals ($O^{2\cdot-}$) as a result of roping the interaction with hydrogen peroxide (H_2O_2) via the Fenton reaction has always been the primary mechanism for igniting nano-noxiousness in Zn doped NiO nanoparticles. The interface of nanoparticles with bacterial and fungi cells is based on the generation of Reactive Oxygen Species (ROS), which react with the microbial cell wall and

rupture the cell membrane, preventing the cell from further growth. Henceforth, bacterial death is thus inevitable resulting in the seepage of intra-cellular components. These nanoparticles feature bactericidal characteristics through the generation of ROS that damage the DNA synthesis, mechanical and metabolic functionalities of a microbial cell, ultimately leading to apoptosis. The bacterial DNA, cell wall, and plasma membrane are critical components of bacterial cells indispensable for survival and growth. The negatively charged nature of DNA, the bacterial cell wall (consisting of negatively charged lipopolysaccharides or teichoic acid), and the plasma membrane (incorporating negatively charged phospholipids) reveal that they are viable targets for positively charged metal oxides [30-31]. Besides, the biological implications of the synthesized NiO nanoparticles are swayed by the crystallinity, i.e., smaller crystallite size nanomaterial perform better antibacterial and antifungal activities. In addition to, the temperature of the precursor solution, the rate of addition and the concentration of gelling agent to the precursor, the solution pH maintained during the growth of the nanoparticles, the concentration of reactants, the nature of the solvents, compositional variability, calcination temperature, and other fundamental decisive factors influence the physical characteristics of NiO nanoparticles and plays a tuning role during the synthesis process. Since the principal physicochemical properties of NiO are governed by its particle morphology and crystallite size, it is vital to synthesize NiO nanomaterials with distinctive aspects, enabling their potency for biomedical and environmental applications [32]. Henceforth, in this work nickel oxide nanoparticles incorporated with varied concentrations of zinc (Zn) were particularly prepared via scalable and economically viable citrate assisted sol-gel strategy buffered through gelling agents at optimum pH promotes tunable energy band gap, and tailored nanoparticle system. The unsurpassed antimicrobial responses of synthesized nanoparticles were systematically studied and it throws a scientific spotlight on environmental remediation applications.

2. Experimental Procedure

2.1. Synthesis

Analytical grade nickel nitrate hexahydrate ($\text{Ni}(\text{NO}_3)_2 \cdot 6\text{H}_2\text{O}$), zinc nitrate hexahydrate ($\text{Zn}(\text{NO}_3)_2 \cdot 6\text{H}_2\text{O}$), citric acid anhydrous ($\text{C}_6\text{H}_8\text{O}_7$), and anhydrous ammonia solution (NH_3) were purchased from Merck, used without further purification. Pure and Zn doped nickel oxide nanoparticles with varying zinc contents (0.1, 0.2, and 0.3 M) were synthesized via an eco-friendly sol-gel citrate method utilizing precipitating agent ($\text{C}_6\text{H}_8\text{O}_7$) for the gelling process. Nickel & zinc nitrate powders taken in the stoichiometric ratios were completely dissolved in double distilled water through a magnetic stirrer and simultaneously citric acid solution was prudently added to arrive at a homogeneous precursor solution. The pH of the above solution was continuously maintained at 7 by slowly introducing NH_3 and the ultimately resulting solution was vigorously stirred at 100 °C for 6 h to acquire a gel, which was then dried in an electrically heated hearth (oven) for 18 h to expel the moisture and intermediately formed ions of $\text{Ni}(\text{OH})_2$. Furthermore, dried samples were annealed at 500 °C for 4 h in the muffle furnace to extract excess hydrate, nitrate ions, and the acquired powders were ground into uniform scaled nickel oxide particles in a nano-meter realm assisted by pestle and mortar. Higher concentrations varied Zn (10, 20, 30%) doped

NiO nanoparticles were successfully synthesized following the analogous approach and the schematic illustration of the synthesis methodology is displayed in Fig 1.

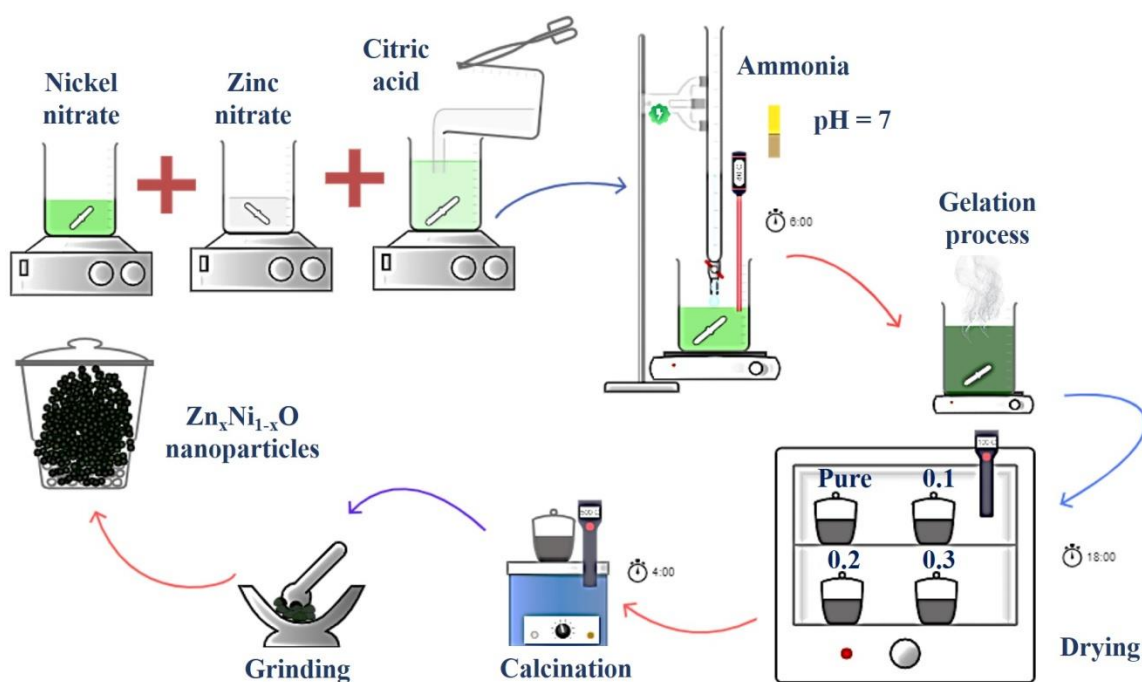


Fig 1. The schematic synthesis procedure of $Zn_xNi_{1-x}O$ ($x=0, 0.1, 0.2, 0.3$) nanoparticles

2.2. Characterization

The as-synthesized Zn doped NiO nanoparticles were attempted to a series of characterizations to investigate its morphology assests, structure, surface chemistry, crystallite size, optical, and magnetic characteristics. The diffraction pattern and the structural features of the nano samples were examined via a high-definition PANalytical X-Ray Diffractometer that uses Bragg-Brentano geometry at an irradiation wavelength of 1.5406 Å (Cu-K α) with a scan step size of 0.084 in the angular range 5–140° in which the working voltage and current were set as 30 kV and 10 mA respectively. SHIMADZU, UV 3600 PLUS was employed to study absorption spectra and bandgap energy of the samples over the wavelength range of 200 to 800 nm using water as the dispersion phase. The vibrational attributes and functional group confirmation of $Zn_xNi_{1-x}O$ nanoparticles were assessed through Perkin Elmer Spectrometer in the mid-infrared region of 400-4000 cm^{-1} . Surface morphology, elemental inspection, and sample purity along with Zn impact on size and shape of the samples were analyzed by EVO MA15 ZEISS microscope coupled with EDX (Energy Dispersive X-ray) analyzer. Pore size distributions of synthesized nanoparticles were examined through Quantachrome Nova 2200e. Magnetic and dielectric characteristics were inspected through Lakeshore VSM 7407 and N4L Impedance analyzer PSM 1735 LCR meter for a constant bias voltage performedat room temperature.

2.3. Antibacterial assay

Antibacterial competence of pristine and different concentrations of zinc incorporated NiO nanoparticles were analyzed using well diffusion approach against various pathogenic bacterial strains which commonly occur in wastewater streams such as gram-positive (*Staphylococcus aureus*, *Enterococcus faecalis*) and gram-negative bacteria (*Escherichia coli*, *Klebsiella pneumoniae*) using the Muller-Hinton Agar (MHA). The bacterial strains such as *S. aureus* (MTCC 96), *E. faecalis* (MTCC 439), *E. coli* (MTCC 443), and *K. pneumoniae* (MTCC 109) were purchased from IMTECH, Chandigarh for the in-vitro antibacterial activity. The precursory action for the study involved 25 ml of MHA coating on the completely sterile glass petri plates and pursuing the overnight agar solidification, the bacterial culture of the given strains was scrubbed on the agar surface. The antibacterial response was estimated at a specific concentration with the required amount of prepared nanoparticles diluting in dimethyl sulphoxide (DMSO) and they were loaded into the wells made using a sterile cork borer with a diameter of 6 mm. Blank disc infused with corresponding solvent was utilized as negative control and azithromycin (30 µg/well) was employed as a positive control to assess the antibacterial efficacy of the synthesized nanoparticles. The plates were incubated in a bacteriological incubator for 24 h at 37 °C after which Zone Of Inhibition (ZOI) was measured for all the samples using antibiotic zone scale.

2.4. Antifungal characterization

The antifungal activity performed by the as-synthesized nanoparticles was tested against two fungal strains such as *Candida albicans* (MTCC 227) and *Aspergillus niger* (MTCC 404) purchased from IMTECH, Chandigarh using the well diffusion method. The completely sterile petri plates (Himedia, Mumbai) were filled with 25 ml of Potato Dextrose (PD) agar. The plates were allowed to solidify after which fungal suspensions grown for three days were made 10^5 cfu/ml of which 100 µl of suspension was swabbed using a sterile swab and the wells were made using a sterile cork borer with a diameter 6 of mm. The test samples dissolved in DMSO were loaded onto the corresponding wells along with DMSO and clotrimazole (30 µg/well) as negative and standard controls respectively. The antifungal capability was estimated by measuring the ZOI using the antibiotic scale zone after incubating the plates for 48-72 h maintained at 37 °C.

3. Results and Discussion

3.1. Structural Analysis

X-Ray Diffraction pattern provides data on the structural specifications, crystallographic facet, defect states and, the impact of doping zinc on the nickel oxide crystal structure. All of the diffraction peaks were precisely indexed to the (111), (200), (220), (311) and (222) planes at the reflected angles (2θ) = 37.36°, 44.54°, 62.90°, 76.35°, and 79.40° respectively. The principal peaks of pristine and zinc doped ($x=0.1, 0.2, 0.3$) nickel oxide nanoparticles correspond to the face-centered cubic structure of NiO with space group (Fm-3m) and fit well with JCPDS card no. 78-0429 with lattice parameter $a = 4.06 \text{ \AA}$ ($=b=c$) [33]. Furthermore, there are no impurity-related peaks, confirming that the zinc ions are effectively incorporated into the NiO host lattice without causing a change in crystal structure or the creation of the ZnO phase. The quality of synthesized nanoparticles and the dispersion

of corresponding compositional phases could be studied by investigating the Full Width at Half Maximum β_{hkl} (FWHM) from the XRD spectra as the crystalline peaks encounter substantial broadening by the consequence of doping as shown in Fig 2 (a). The average crystallite size (D) and the lattice parameter (a) is estimated employing the highly intense preferential plane (200) based on the Scherrer equation,

$$D = \frac{k\lambda}{\beta_{hkl}\cos\theta_{hkl}} \quad (1)$$

$$a = d(h^2 + k^2 + l^2)^{1/2} \quad (2)$$

Where k denotes the shape factor (~ 0.9), λ is the X-ray wavelength (1.5406 Å), θ corresponds to the Bragg angle denoting the most dominating peak, and d refers to the interplanar spacing ($d = \frac{\lambda}{2\sin\theta}$).

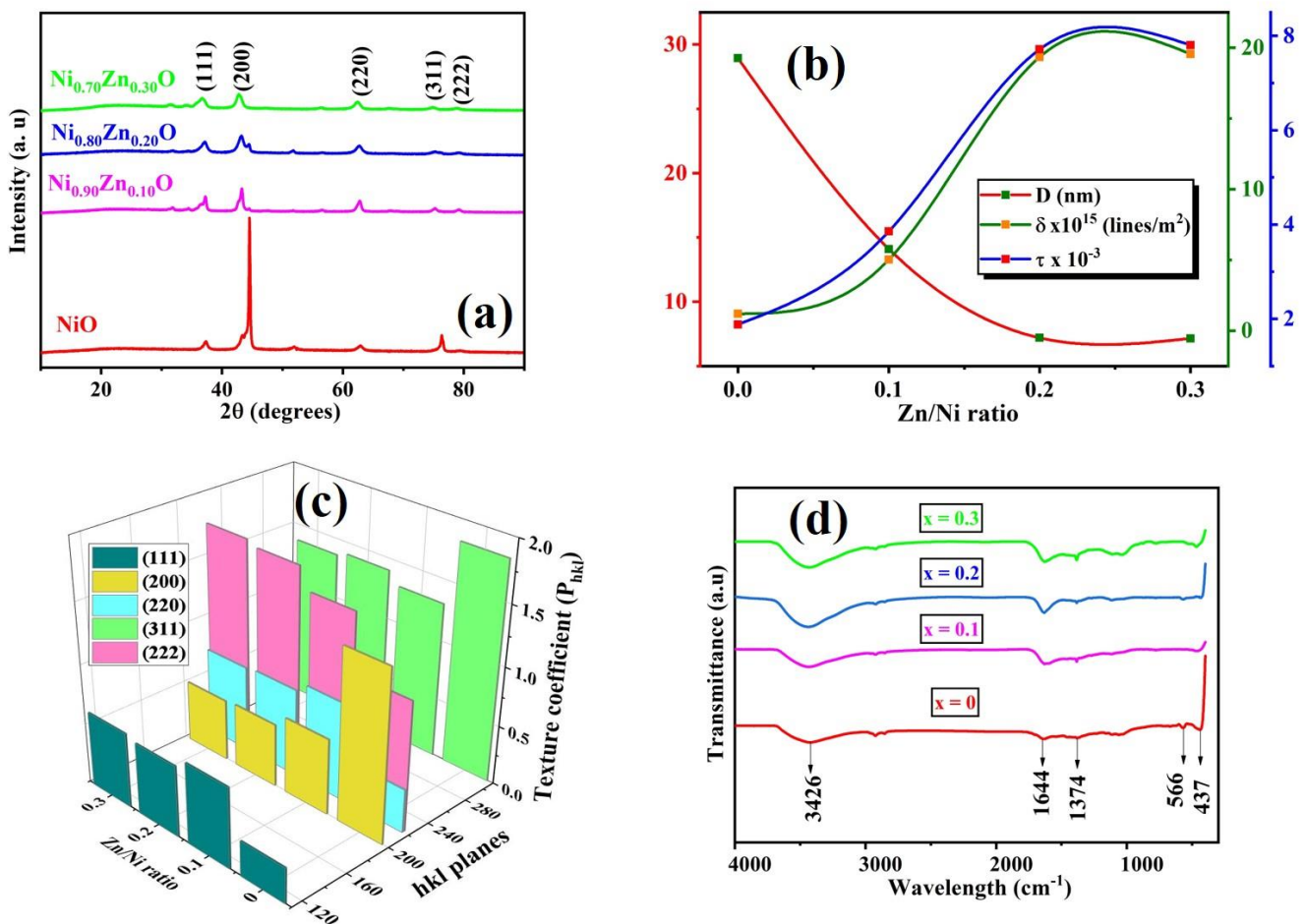


Fig 2. (a) XRD pattern of Zn d(b) Variation of D , δ , and τ as a function of Zn content

3.1.1. Measurement of different microstructural parameters

The deviations developed in the nanomaterial as expressed by Williamson and Smallman [34] is the dislocation density (δ) and the irregularities created in the stacking of

atomic planes of substituting zinc into the nickel lattice is termed as stacking fault (τ) and are calculated as,

$$\delta = \frac{1}{D^2} \quad (3)$$

$$\tau = \left[\frac{2\pi^2}{45 (3 \tan\theta)^2} \right] \beta \quad (4)$$

The X-Ray density (ρ_X) of the synthesized particles in the nano regime are evaluated as,

$$\rho_X = \frac{4M}{Na^3} \quad (5)$$

Where N refers to the Avogadro number ($6.023 \times 10^{23} \text{mol}^{-1}$) and M is the molecular weight of the sample.

The preferred orientation of the nanoparticles represents the texture of a particular (hkl) planes analyzed through the Harris model termed as texture coefficient (P_{hkl}) [35] and it is given as

$$P_{hkl} = \frac{I(hkl)}{I_0(hkl)} / \frac{1}{n} \sum_{i=1}^n \frac{I(hkl)}{I_0(hkl)} \quad (6)$$

$I_0(hkl)$ and $I(hkl)$ denotes the standard intensity from the reference NiO and experimentally observed intensity of synthesized nanoparticles respectively, n refers to the reflection number of the measured planes. A specimen has zero texture ($P_{hkl} = 0$) if all of its orientations are random and moderate or strong texture coefficient ($P_{hkl} > 1$) if the particles have a particular preferred orientation. Fig 2 (b) shows the variation of microstructural parameters with the zinc content and Fig 2 (c) depicts the texture coefficient with different dopant concentrations of zinc and it is evident that crystal planes (311) and (222) exhibits P_{hkl} greater than unity. The number of crystallite size reveals a reduction of crystallinity with increasing Zn concentration from 0 to 30 % and the lattice parameter shows an increasing trend with doping. The incorporation of dopant atoms strain the host lattice, leading to a shift in lattice parameter readings and a minor shift in the associated peaks to higher or lower angles. The substitution of Ni^{2+} atoms with lower ionic radii (0.69 Å) for Zn atoms with larger ionic radii (0.74 Å) may potentially explain the decline in crystallite size and rise in the related lattice parameter [36]. In addition, the crystallite size of synthesized samples is influenced by changes in Zn^{2+} concentration, the prevalence of defects caused by synthesis temperature. Lesser the crystallite size, higher the lattice strain and higher is the effect of surface atoms [37]. The atoms in grain boundaries create a stress field that promotes lattice strain, as a result stress field-induced lattice deformities existing in the grain boundaries could cause a considerable increase in lattice strain in zinc doped nickel oxide nanoparticles in comparison with the higher crystallite size of pure nanoparticles. Dislocation density, stacking fault, surface area, and other microstructural parameters calculated are tabulated in Table 1.

$Zn_xNi_{1-x}O$	D (nm)	a (Å)	d (Å)	$\delta(10^{15})$ (lines/m ²)	Stacking fault(τ) (10 ⁻³)	X-ray density (ρ_x) (g/cm ³)
$x=0$	28.94	4.06	2.03	1.19	1.88	7.37
$x=0.1$	14.10	4.17	2.08	5.02	3.85	6.86
$x=0.2$	7.19	4.18	2.09	19.34	7.71	6.89
$x=0.3$	7.15	4.22	2.11	19.56	7.80	6.76

Table 1. Microstructural parameters of Zn doped NiO nanoparticles

3.3. Spectroscopic Analysis

Fourier-transform infrared spectroscopy is used to analyze the chemical composition and vibrational frequencies of diverse functional groups extant in the synthesized samples by monitoring the molecular vibrations emitted by the atoms of the specimen. Fig 2 (d) displays the full sweep transmittance spectra of pure and Zn (0.1-0.3 M) doped nanoparticles having several significant peaks which have been recorded in the realm of 4000 to 400 cm⁻¹ at room temperature. In the lower wavenumber domain of the spectra (500–700 cm⁻¹), the narrow summits are correlated to the typical characteristics peaks of metal-oxygen (M-O) and metal-hydroxide (M-OH) bonds. As a result, the Ni-O stretching vibrational mode is recorded at 437 cm⁻¹ corresponding to the transverse mode of vibration (T-O) and the peak at 566 cm⁻¹ represents the longitudinal vibrational mode (L-O) of NiO. The band at 1374 cm⁻¹ confirms the existence of CO₂ molecules adsorbed from the environment and the weak absorption band in the vicinity of 1644 cm⁻¹ was consigned to bending vibrational mode of water molecules present on the nanoparticle surface as a result of H-O-H adsorption in the air atmosphere during the calcination process [38]. Broadband at 3426 cm⁻¹ is attributable to O-H stretching vibrations of H₂O and OH groups which is relative to the proportion of H₂O molecules trapped by nickel oxide particles signifying that the nanoparticles retain higher surface area. The force constant and bond length of Ni and O atoms in the synthesized samples were effectively estimated through the T-O mode as [39],

$$\omega^2 = \left(\frac{1}{2\pi c}\right)^2 \left(\frac{k}{\mu}\right) \quad (7)$$

Where ω and k refers to the wavenumber of transverse mode of vibration and force constant. μ can be calculated from atomic weights of NiO as,

$$\mu = \left(\frac{M_{Ni}M_O}{M_{Ni} + M_O}\right) \quad (8)$$

Bond length r can be estimated from the force constant from the expression,

$$k = \frac{17}{r^3} \quad (9)$$

The elastic parameters computed from the spectroscopy analysis are given in Table 2 and it is noted that the bond length reduces as the transverse mode wavenumber increases due to a

surge of Zn ions in the NiO molecules. This spike in transverse mode wavenumber clearly confirms blue shift which is in accordance with optical results.

Zn/Ni ratio	T-O peak (cm^{-1})	μ (10^{-26} kg)	k (N/cm)	r (Å)
0	437	2.0874	1.3619	2.3197
0.1	441	2.0924	1.3900	2.3039
0.2	433	2.0974	1.3802	2.3094
0.3	457	2.1023	1.4729	2.2599

Table 2. Force constants and bond lengths estimated from FTIR spectra

3.2. Morphological analysis

Surface morphological properties of $Zn_xNi_{1-x}O$ ($x = 0, 10, 20,$ and 30 wt. %) nanoparticles were examined by scanning electron microscopy technique and the images are displayed in Fig 3.

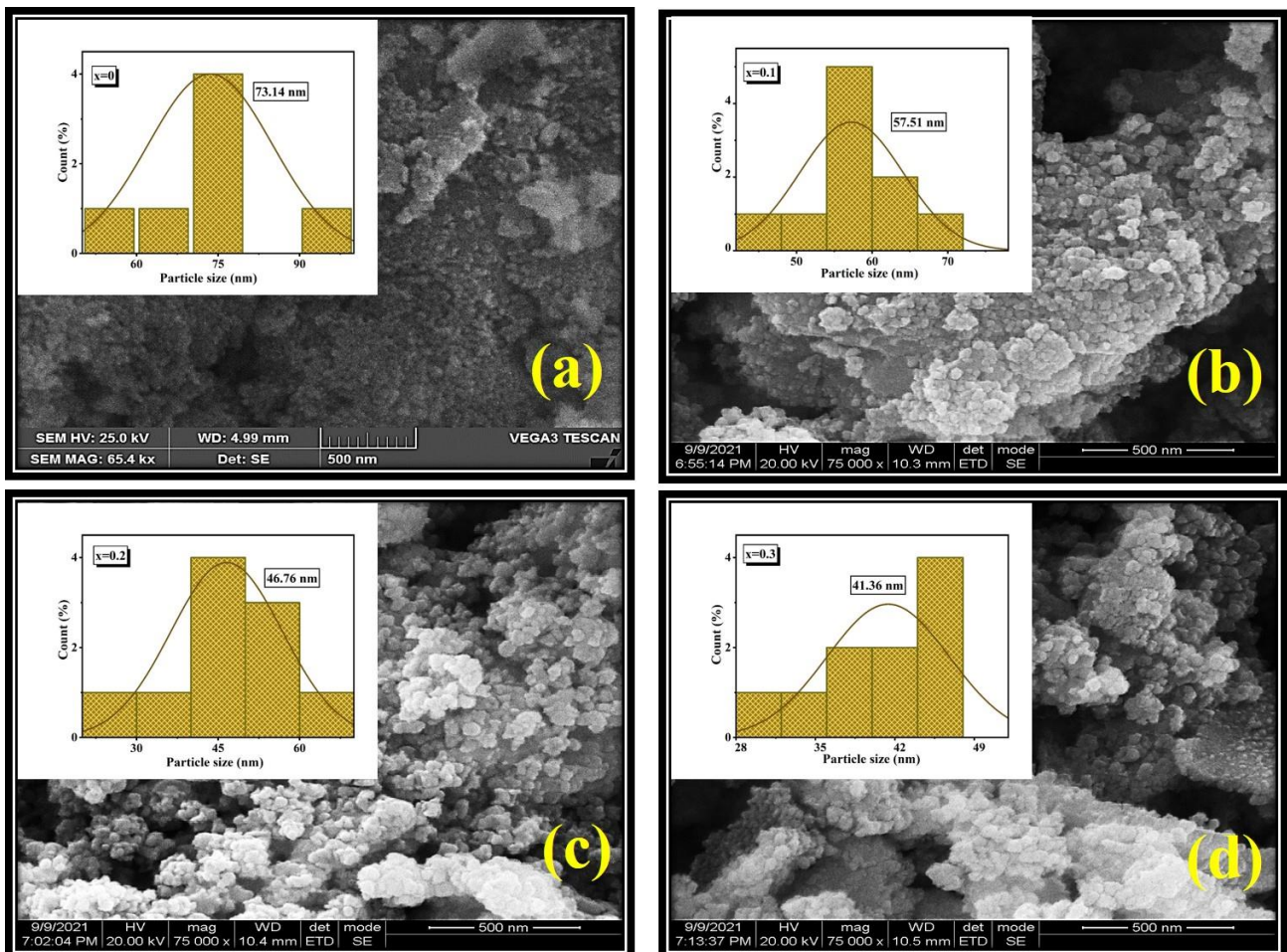


Fig 3. SEM images of $Zn_xNi_{1-x}O$, $x =$ (a) 0.00 (b) 0.10 (c) 0.20 (d) 0.30 M (inset: Histogram images)

The SEM images show that nanoparticles form a spherical configuration, and the agglomeration observed in samples occurs as the zinc concentration in NiO hikes, which is caused by to the reduced particle size of Zn doped nickel oxide nanoparticles. The nanoparticles develop an affinity to clump together to lower the elevated surface energy created by the higher surface to volume proportion. The particle size of the nanoparticles was estimated and the histogram images are shown in the inset of Fig 3. It is notified that the dopant introduced in NiO nanoparticles significantly influences the growth process and hence the particle size and shape of the synthesized nanoparticles would be impacted by zinc inclusion [40]. Particle size decreases from 73 to 41 nm as doping the NiO lattice with zinc atoms. Fig 4 presents the EDX spectra and complete elemental composition (inset) of NiO nanoparticles doped with various amounts of zinc. The spectra verified the existence of just Ni, Zn, and O as fundamental constituent particles in products, with no other metals present, proving that no additional secondary particles or contaminants are formed during the synthesis process [41].

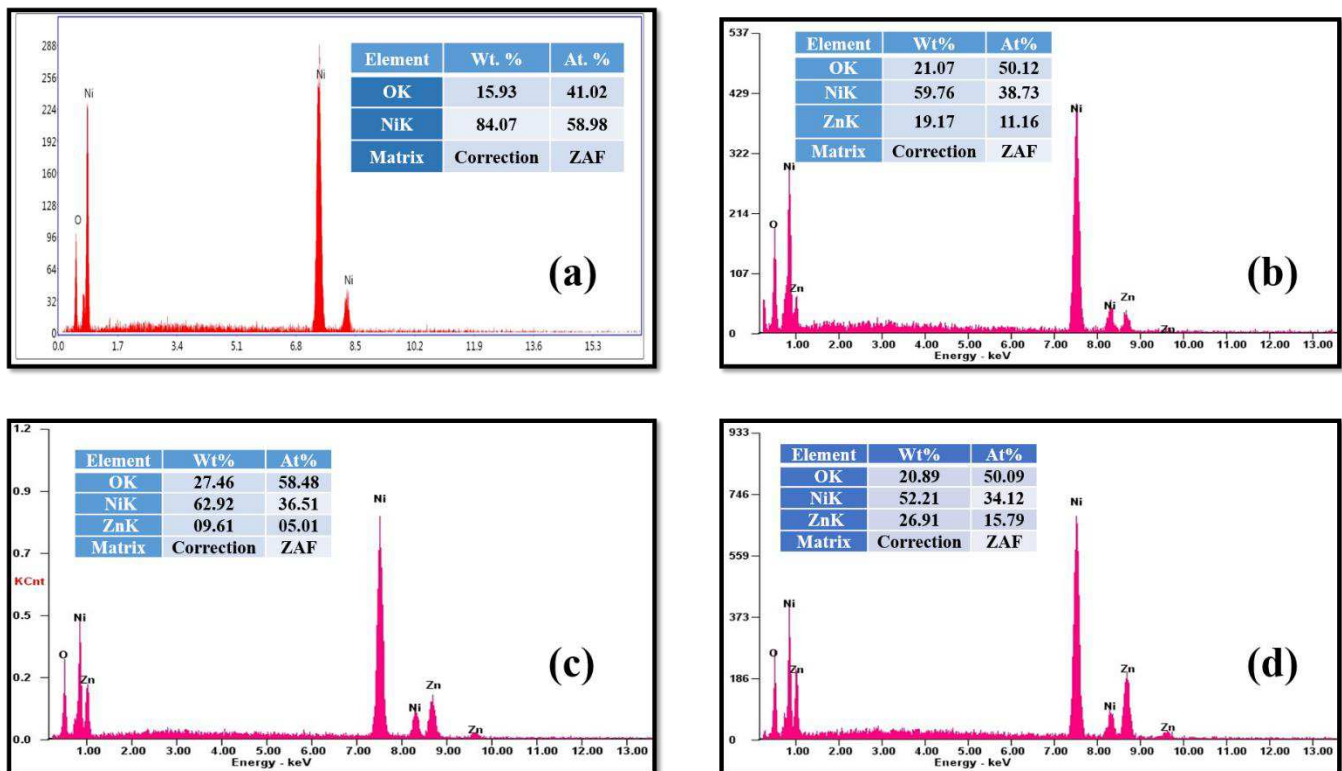


Fig 4. EDX spectra of Zn_xNi_{1-x}O, x = (a) 0.00 (b) 0.10 (c) 0.20 (d) 0.30

3.4. Optical Analysis

3.4.1. Determination of energy bandgap

The optical aspects of Zn incorporated NiO nanoparticles are investigated to determine the effect of zinc doping on absorbance (A %) over the wide wavelength spectral span of 200–800 nm as shown in Fig 5 (a). A broad absorption band is spotted in the wavelength continuum of 300 – 400 nm explicable to a transition of nickel oxide from valance to

conduction band. The optical bandgap (E_g) can be credibly calculated applying Tauc's equation [42] which relates the absorption coefficient to bandgap energy as,

$$\alpha h\nu = A(h\nu - E_g)^n \quad (10)$$

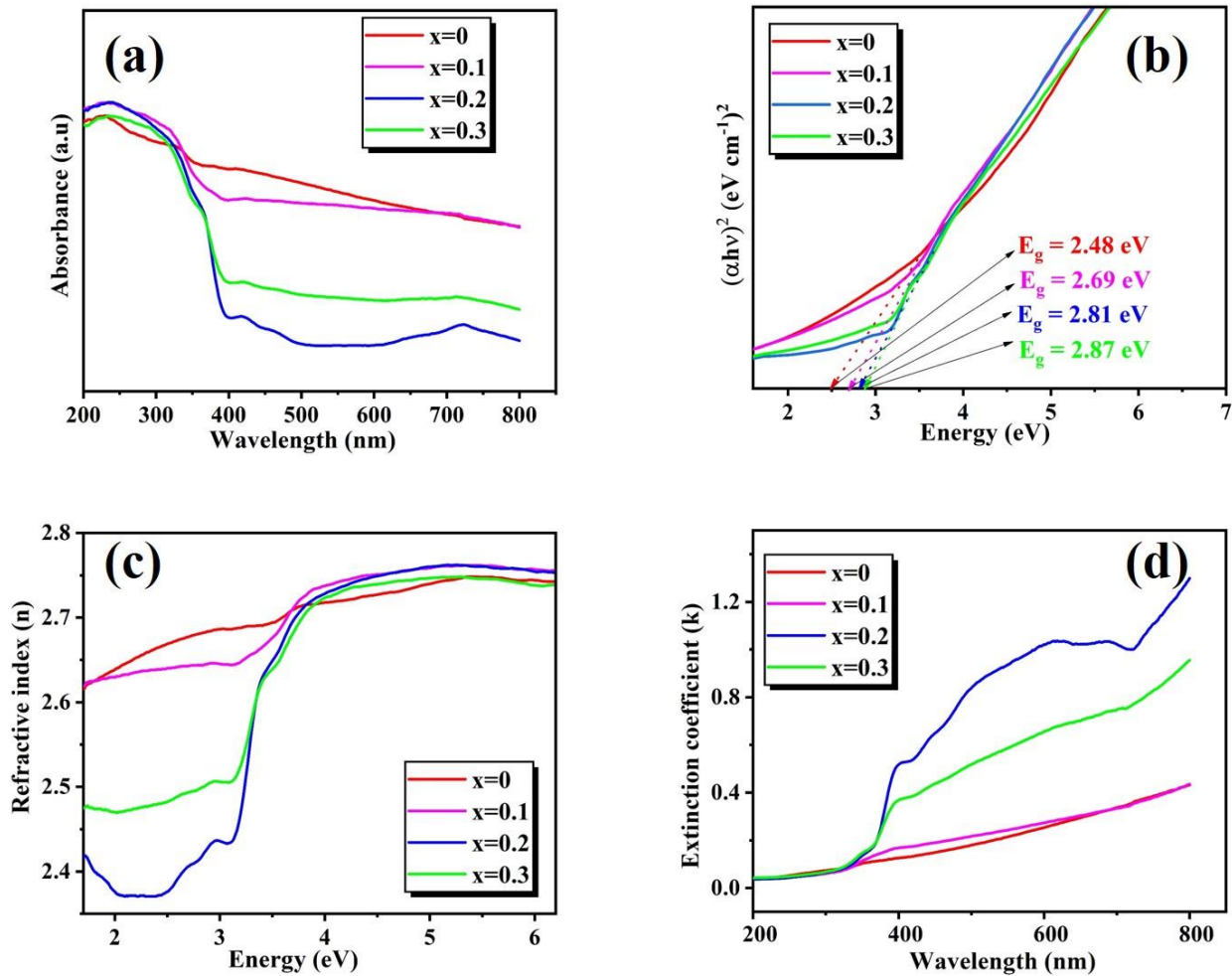


Fig 5. (a) UV-vis absorption spectra (b) Bandgap energy (c) n Vs energy (b) k Vs wavelength of Zn doped NiO nanoparticles

Where α , $h\nu$, and E_g refer to absorption coefficient, frequency of photon energy, incident energy of incoming photons, and optical band gap energy respectively. A denotes transition probability and n refers to an empirical number where $n = 1/2$ and 2 for direct and indirect allowed mode of transitions respectively [43]. Fig 5 (b) delineates optical band gap energy estimated from equation (10) where it is examined that E_g increases from 2.48 to 2.87 eV as the dopant discrepancy intensifies. It is clearly demonstrated that as Zn concentration (0-30 wt. %) in nickel oxide lattice elevates, band gap energy increases accounting to the progression of blue shift. This expansion in band gap as a factor of Zn concentration is possibly impelled by the substitution of the Zn^{2+} ion at the Ni position, which releases more number of electrons and promotes defects to be constrained, as explained by the Burstein Moss shift (ΔE) [44]. When Ni^{2+} ions are replaced by Zn^{2+} ions, then free electrons are

generated in the NiO lattice network causing an increase in the carrier concentration which in turn leads the electrons to drive from the Fermi energy level towards the conduction band which promotes the conductivity by supplying electron energy levels. Thus the additional charge carriers provided by the donor Zn^{2+} ions cause the Fermi energy level to move towards the conduction band, ultimately resulting in a wider optical band gap. The tailoring of the optical band gap is connected with structural characteristics such as crystallite size and micro-strain effect, which is known as the quantum size confinement. The inverse relationship between crystallite size and optical band gap as expressed by Marotti's is given as [45],

$$E(R) = E_g(\alpha) + E_b \left(\frac{\pi a_B}{R} \right)^2 \quad (11)$$

$E_g(\alpha)$ is the energy bandgap of bulk material, E_b refers to exciton binding energy, a_B is the exciton Bohr radius in the range of 6.6-28.7 nm. A blue shift is observed when the crystallite size is less than Bohr's excitonic radius. The quantum size and blue shift effect can be detected since the (200) preferred orientation peak crystallite size is less than Bohr's radius and so the optical band gap varies with the corresponding orientation.

3.4.2. Optical dispersion parameters

The analysis of optical dispersion parameters is considered as a crucial component in the design of numerous electronic devices which can be utilized in a variety of application fields including telecommunications, electricity, filtration, electrical buttons, opto-electronics, photonics, and cable applications [46]. The extinction coefficient (k) is imperative in optical evaluations of electromagnetic waves that have been absorbed in the medium and lost as a result of scattering. It is given as,

$$k = \frac{\alpha \lambda}{4\pi} \quad (12)$$

Where $\alpha = \frac{(1-R)^2}{2R}$ is the absorption coefficient, a parameter which measures total optical losses produced by absorption and scattering inside the material. The refractive index (n) dispersion plays a pivotal role in optical materials research since it is a decisive determinant in the field of optical communication and engineering equipment for spectral dispersion. It is related with the reflection (R) factor and extinction coefficient as [47],

$$n = \frac{1+R}{1-R} + \sqrt{\frac{4R}{(1-R)^2} - k^2} \quad (13)$$

Here $R = 1 - (T * e^A)^{0.5}$, T is the transmission factor of the material.

Fig 5 (c) and (d) illustrates the wavelength (energy)-dependent refractive index and extinction coefficient of pure and Zn doped NiO with varied doping concentration. It is distinct that the real refractive index (n) reaches its maximum value at the lower wavelength region or at higher energy ($h\nu$) and drops monotonically as the wavelength increases, exhibiting normal dispersion behaviour. Similarly, a higher magnitude of extinction coefficient (k) in higher wavelength region ($\lambda > 450 \text{ nm}$) can be justified by the metallic nature of nanomaterial and the decrease in k with wavelength (300-450 nm) can be correlated to light absorption in this

range readily. The complex dielectric constant ($\varepsilon = \varepsilon_r + \varepsilon_i$) is associated with the electronic structure and excitation of primary electrons in as-synthesized nanoparticles and it is a fundamental quantity that defines the relationship between the fabrication of potent optoelectronic peripherals. It examines a permittivity and polarizability of a material in relation to the density of states within the forbidden energy gap. The real part (ε_r) of the dielectric constant indicates the speed of light that may be slowed down in the material and the imaginary part (ε_i) specifies the energy absorbed by an electric field on account of dipole mobility and interaction [48]. They are computed as follows,

$$\varepsilon_r = n^2 - k^2 \quad (14)$$

$$\varepsilon_i = 2nk \quad (15)$$

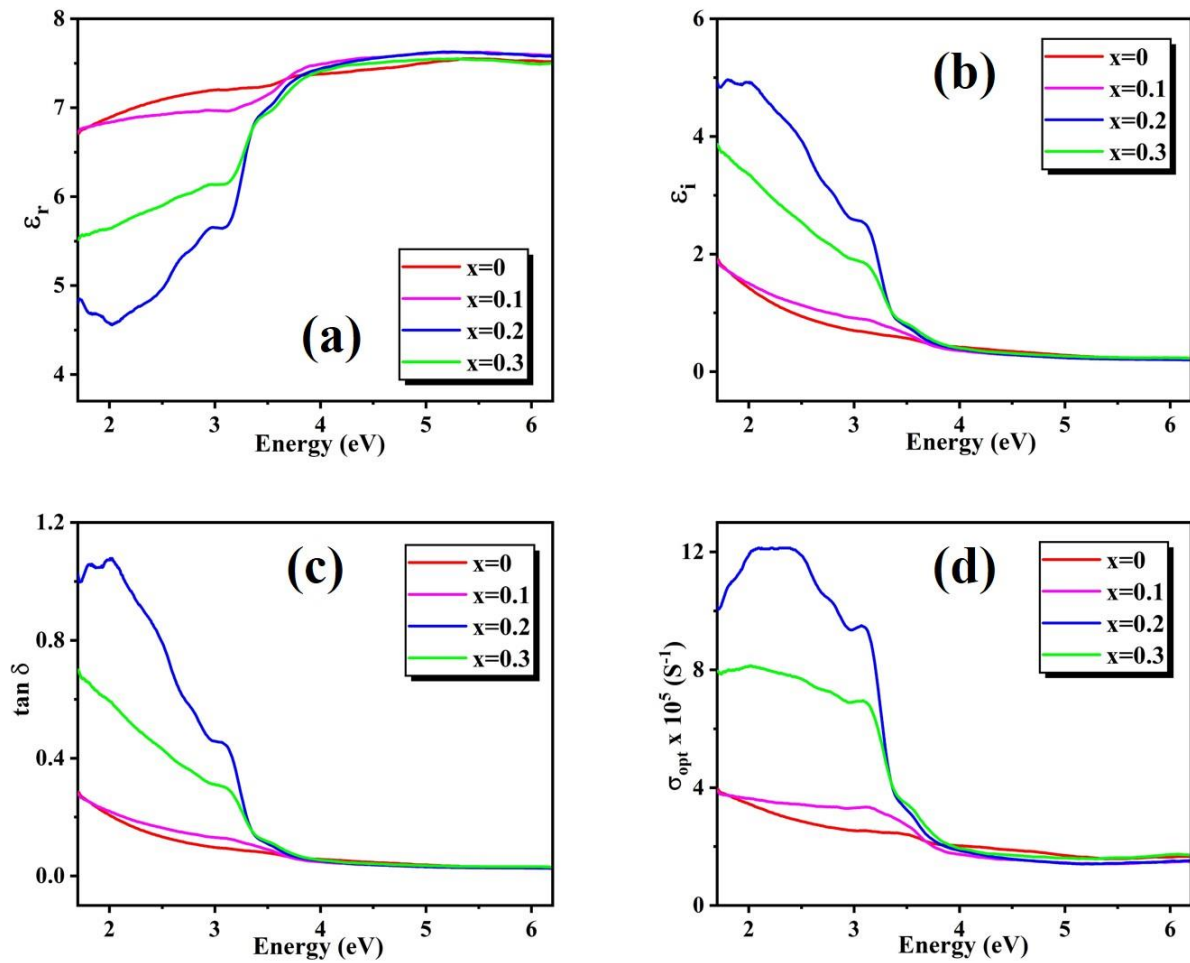


Fig 6. (a) ε_r (b) ε_i (c) $\tan \delta$ (d) σ_{opt} Vs energy of pure and Zn doped NiO nanoparticles

It is certain that the spectral distribution of ε_r possess a similar trend as the real part of the refractive index (n), while the spectral pattern of ε_i follows the same behaviour of extinction coefficient as shown in Fig 6 (a) and (b). The data of ε_r and ε_i of dielectric constant taken into consideration to analyze the statistics of dielectric loss ($\tan \delta$) which is estimated from the ratio of ε_i and ε_r via the following formulation,

$$\tan \delta = \frac{\varepsilon_i}{\varepsilon_r} \quad (16)$$

The optical response of a material generated by the movement of charge carriers upon incoming electromagnetic waves exposure is termed optical conductivity (σ_{opt}) and it is dependent on several significant factors such as absorption coefficient, refractive index, the velocity of light, and photon energy [49]. Fig 6 (c) and (d) depicts the variation of dielectric loss and optical conductivity of undoped and concentration varied Zn incorporated nickel oxide nanoparticles and it is given as,

$$\sigma_{opt} = \frac{anc}{4\pi} \quad (17)$$

It is observed that optical conductivity elevated exponentially up to ~ 2 eV for all synthesized samples. This rise could be linked to a substantial rise in the absorption coefficient in this region or photon energy absorbed by nanoparticles excite the charge carriers from valance to conduction band. The SELF (Surface Energy Loss Function) and VELF (Volume Energy Loss Function) are related to the energy loss of incident electromagnetic waves experienced by electrons existing in a material or on a surface. The real and imaginary parts of dielectric constants are closely connected with the energy loss functions (SELF and VELF) [50] as follows,

$$SELF = \frac{\varepsilon_r}{(\varepsilon_r + 1)^2 + \varepsilon_i^2} \quad (18)$$

$$VELF = \frac{\varepsilon_i}{\varepsilon_r^2 + \varepsilon_i^2} \quad (19)$$

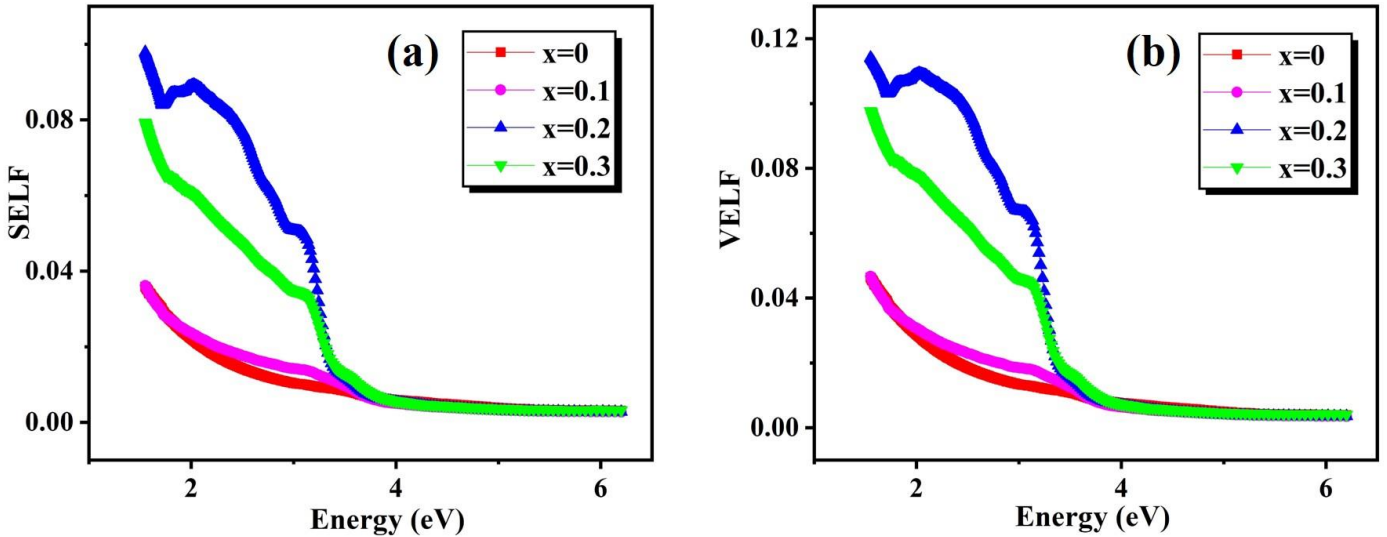


Fig 7. (a) SELF (b) VELF Vs energy of synthesized nanoparticles

The intrinsic energy loss of the fast-moving electrons which transport the surface and bulk of the material is proportional to SELF and VELF respectively. Thus the SELF and VELF of any optical dielectric medium are vital parameters for the device in an optical communication system. Both SELF and VELF measurements decrease as photon energy increases for all

resultant nanoparticles as depicted in Fig 7 (a) and (b) and it is noted that SELF is less than VELF as the electron mobility within a material is controlled by the agglomerate of clusters.

3.4.3. Dispersion of energy parameters

The principal parameters of dispersion energy factors that influence lattice absorption include single effective oscillator energy (E_0) and effective dispersion energy (E_d) of pure and zinc doped nickel oxide nanoparticles are discussed to encounter its suitability for fabricating optical materials in spectral dispersion and optical communications. Wemple and DiDomenico (WDD) proposed a single oscillatory model to extract various energy dispersion parameters from the refractive index expressed as a function of energy as [51-52],

$$\frac{1}{n^2-1} = \frac{E_0}{E_d} - \frac{1}{E_0 E_d} (h\nu)^2 \quad (20)$$

E_0 is the energy separation between the centers of both the conduction and valance bands of nanomaterials while E_d is connected to the structural traits of the materials, such as ionicity, anion valency, and coordination number of the atoms, which quantifies the average strength of interband optical transitions. The single oscillator energy and dispersion energy are obtained by plotting $(h\nu)^2$ along the X-axis and $(n^2 - 1)^{-1}$ along Y-axis as shown in Fig 8. The slope and intercept of the curves determine the parameters of equation (20) by performing a linear fit. The ratio of E_0 decrease with the increase of Zn content which could be ascribed to the decline in the number of scattering centres and enhancement in the band gap energy. In addition, E_d decreases from 46 to 17 eV with respect to zinc concentration and it is attributed to the structural disorder and poor crystallinity of synthesized nanoparticles. The relationship of the energy components E_0 and E_d is engaged to account for the lattice energy (E_L), which confers information about the strength of bonding in an ionic compound is formulated as,

$$n^2 - 1 = \frac{E_d}{E_0} - \frac{E_L^2}{E^2} \quad (21)$$

A graph is plotted between $n^2 - 1$ and E^{-2} where E_L is extracted from the linear part of the slope as shown in Fig 9 (a). The recorded E_L parameter has been noticed to raise as Zn content increases denoting the development in the strength of the bonds. Fig 9 (b) depicts the variation of oscillator and dispersion energy with Zn content in NiO nanoparticles and it is observed that both the energies decrease as zinc concentration increases. The oscillator strength (f), linear static refractive index (n_0) and static dielectric constant (ϵ_s) of pure and concentration varied zinc incorporated NiO nanoparticles were evaluated as [53]

$$f = E_0 E_d \quad (22)$$

$$n_0 = \sqrt{1 + \frac{E_d}{E_0}} \quad (23)$$

$$\epsilon_s = n_0^2 \quad (24)$$

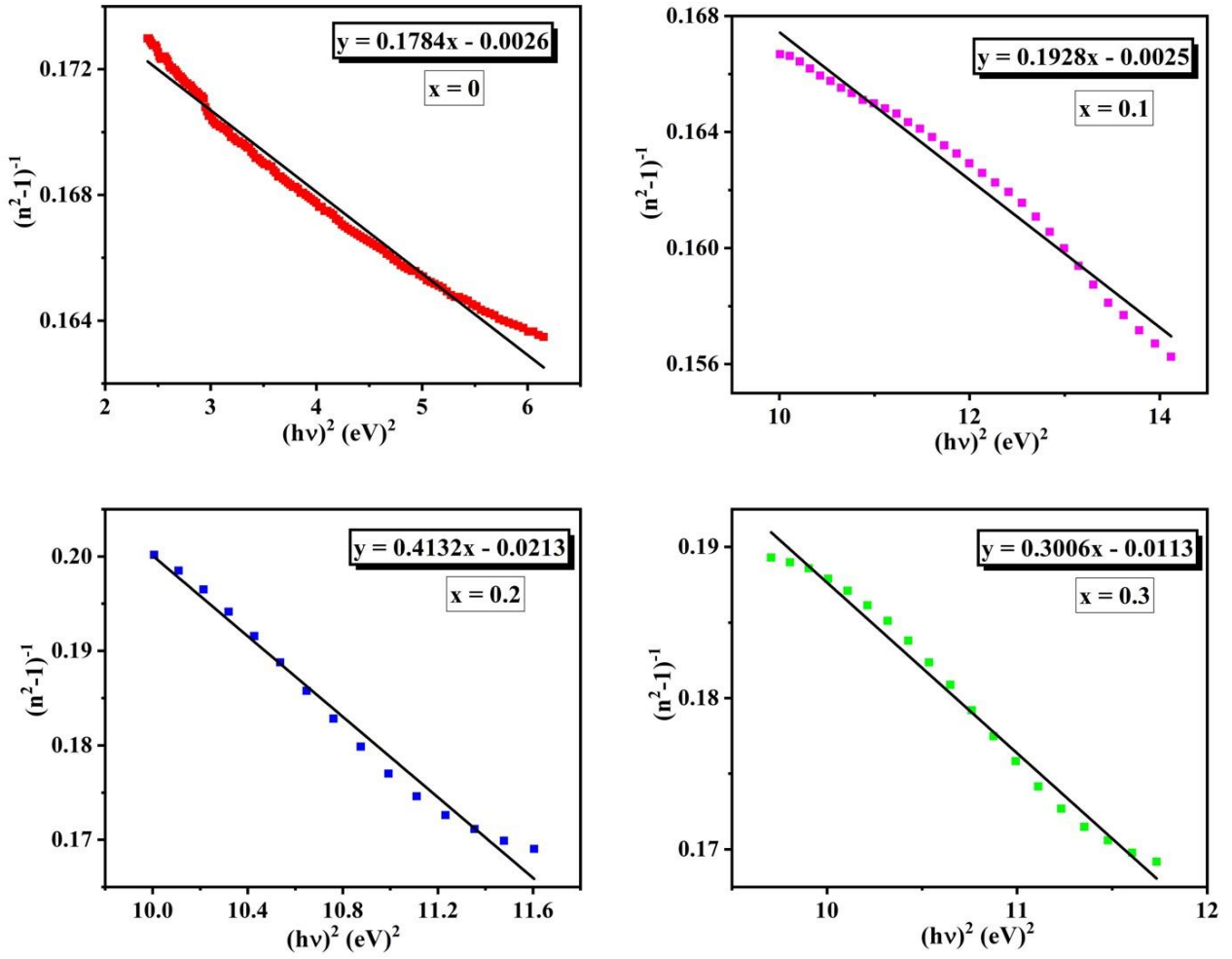


Fig 8. Variation of $(n^2 - 1)^{-1}$ as a function of $(hv)^2$

The optical spectrum moments reflect the dielectric constant and density of valance electrons of the optical materials. The moments of the optical spectrum M_{-1} and M_{-3} are modified and related to dispersion parameters as [54],

$$M_{-1} = \frac{E_d}{E_0} \quad (25)$$

$$M_{-3} = \frac{E_d}{E_0^3} \quad (26)$$

Polarizability measures the degree to which a bound electron responds to an external electric field. The Lorentz-Lorenz equation which connects molar refraction R_m to refractive index n_0 and molar volume V_m is given as,

$$R_m = \left(\frac{n_0^2 - 1}{n_0^2 + 2} \right) V_m \quad (27)$$

Where $V_m = \frac{M}{d}$, M and d represents the molecular weight and density of synthesized nanoparticles. Molar polarizability α_m is directly proportional to molar refraction R_m as,

$$\alpha_m = \frac{R_m}{2.52} \quad (28)$$

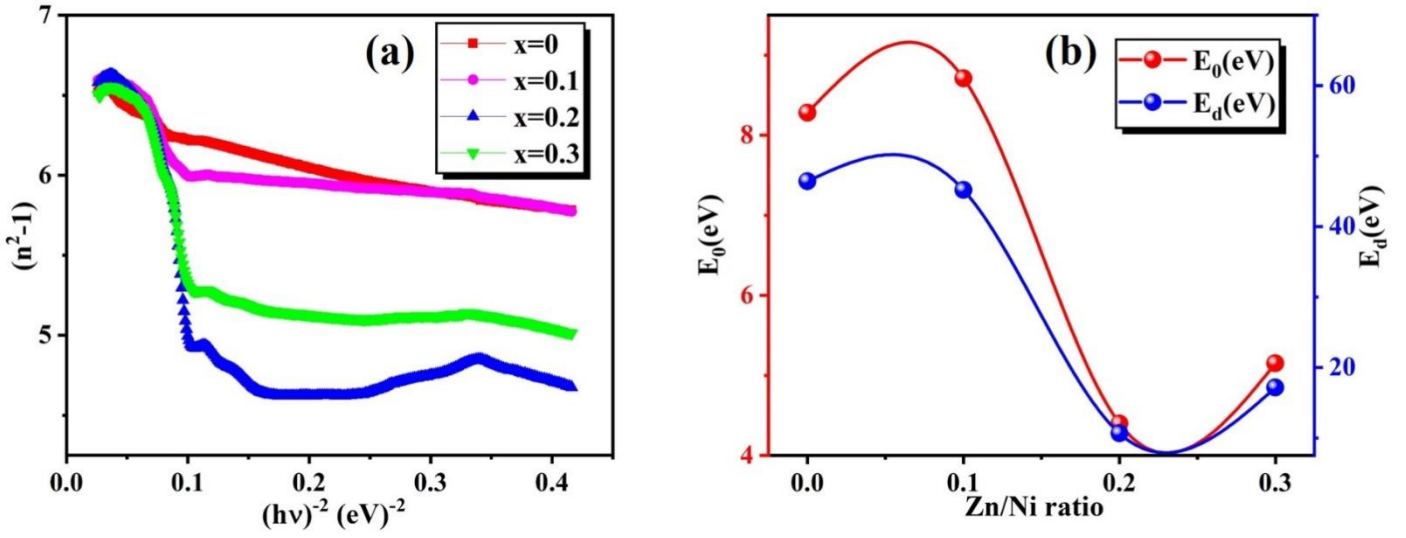


Fig 9. (a) Variation of $n^2 - 1$ as a function of $(hv)^{-2}$ (b) Energy dispersion parameters Vs Zn content

3.4.4. Non-linear optical parameters

The non-linear properties of nanomaterials are estimated to examine the material performance in industries, such as sensors and communications and in the field of optoelectronics that deals with frequency doubling and tripling, data storage, conversion, and transformation. The first ($\chi^{(1)}$) and third order susceptibility of pure and zinc doped nickel oxide nanoparticles are evaluated as [55-56],

$$\chi^{(1)} = \frac{E_d}{4\pi E_0} \quad (29)$$

$$\chi^{(3)} = A(\chi^{(1)})^4 \quad (30)$$

Where A refers to the frequency-independent constant which is equal to $1.7 \times 10^{-10} esu$.

Zn/Ni ratio	E_0 (eV)	E_d (eV)	E_L (eV)	f (eV) ²	n_0	ϵ_s	$\chi^{(1)}$	$\chi^{(3)}$ (10 ⁻¹²) (esu)	n_2 (10 ⁻¹⁰) (esu)	M_{-1}	M_{-3} (eV) ⁻²	R_m (cm ³ /mol)	α_m (Å ³)
0	8.28	46.42	1.383	384	2.59	6.60	0.44	6.72	0.98	5.62	0.081	6.59	2.61
0.1	8.71	45.18	1.388	393	2.48	6.18	0.41	4.94	0.75	5.18	0.068	6.94	2.75
0.2	4.40	10.65	2.238	46	1.84	3.42	0.19	0.23	0.04	2.42	0.124	4.92	1.95
0.3	5.15	17.15	1.964	88	2.07	4.32	0.26	0.83	0.15	3.32	0.125	5.95	2.36

Table 3. Variation of energy dispersion, linear and non-linear parameters with Zn content

The non-linear refractive index (n_2) is related to linear refractive index and third order susceptibility as,

$$n_2 = \frac{12\pi\chi^{(3)}}{n_0} \quad (31)$$

Table 3 summarises the estimated energy dispersion, linear and non-linear parameters of synthesized samples and it is imperative to analyze these quantities for devise fabrication and in opto-electronic applications.

3.4.4. Determination of Urbach energy and electronegativity

The absorption coefficient (α) fluctuated by corresponding incident photon energy to absorption edge has one of the exponential zone known as the Urbach region which is used to identify the nature of localized band tailing width states and is associated with the structural disorderliness of the synthesized nanoparticles. The band structure of the Burstein shift is depicted in Fig 10 (a). The generation of disorderliness is witnessed during the transition from valance to conduction band based on the absorption of photon energy that could be directly attributable to localized tail states produced by defects in as-synthesized nanoparticles, allowing the density of states to tail into the band gap, known as Urbach tail, and the corresponding localized tail energy as Urbach energy shown in Fig 10 (b).

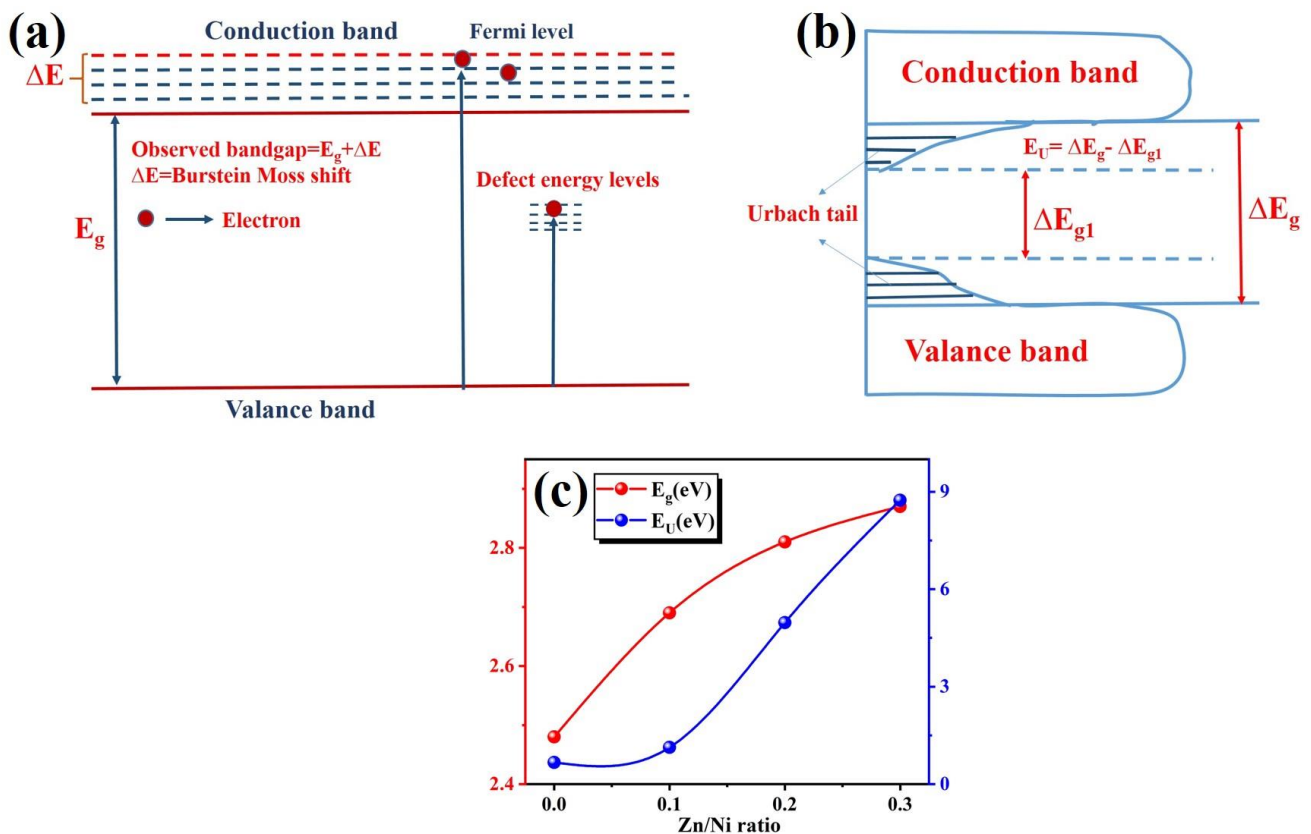


Fig 10. Band structure with (a) Burstein Moss shift (b) Urbach tail (c) Variation of E_g , E_U with Zn content

Urbach rule is given by the relation,

$$\alpha = \alpha_0 \exp\left(\frac{h\nu}{E_U}\right) \quad (32)$$

Where E_U , α and α_0 denotes the Urbach energy, absorption coefficient and constant respectively. Urbach energy is calculated by taking the inverse slope of the linear portion of alpha versus photon energy. Urbach energy increases with an increase in the dopant concentration which manifests that the defects of density and structural disorders in the synthesized samples elevates with the Zn content [57-58]. It is distant that the Urbach energy of 0.3 % Zn doped NiO nanoparticles showcase higher quantity in comparison with other less dopant concentrations, inferring that it has generated a significantly higher number of defects.

3.5. Dielectric studies

Dielectric characterization is a significant study that is conducted to fetch information about structural modifications, transport mechanism, and defect nature of pristine and zinc-doped NiO nanoparticles focussed on the electrical response of materials as a function of frequency ranging from 1 μ Hz to 5 MHz. The dielectric constant is determined by the vector's distinctive degree of polarisation and the orientation of the molecules. The measure of the intensity of electrostatic binding between the ions in any direction of the medium accounts for the dielectric constant. The higher the dielectric constant, the higher will be the electrostatic binding intensity and hence elevated lattice energy. The sample is positioned between two copper electrodes with silver coating on both sides to mimic the operation of a parallel plate capacitor. Dielectric constant versus linearly fluctuating frequency is plotted in Fig 11 (a) and it is estimated via the relation,

$$\epsilon_r = \frac{Cd}{A\epsilon_0} \quad (33)$$

Where C , d , A and ϵ_0 denote capacitance, pellet thickness, area, and vacuum dielectric constant respectively. All the samples exhibit a high dielectric constant at a lower frequency and rapidly decrease when frequency intensifies. At lower frequencies, dipoles smoothly enforce changes in the electric field, but at higher frequencies, dipoles struggle to follow the external electric field, as predicted by the Maxwell-Wagner and Koops phenomenological theory [59]. Atoms dwell in grains and grain boundaries, and the high dielectric constant function in small nanoparticles is attributable to nanograins that act as nano dipoles in the presence of an applied field. According to the theory, the dielectric medium is supposed to be composed of effectively conducting grains separated by poorly conducting or resistive grain boundaries. When an external electric field is applied, charge carriers can freely shift within the grains but accumulate at the grain thresholds acting as a potential obstacle for them, resulting in interfacial polarization. This process could generate large polarisation and thus a lot of dielectric constants are existing at lower frequencies. The observed decrease in dielectric constant with accruing frequency is linked to any species contributing to the polarizability lagging behind the applied field at higher frequencies. Dipoles are unable to pursue the alternating field beyond a certain frequency, resulting in frequency-independent dielectric action. In the present study, the particle size of $Zn_xNi_{1-x}O$ decreases with an increase in x content ($x=0.1-0.3$) increasing the grain boundary. This may denote that

interface polarization of synthesized nanoparticles dominates over the grain boundary effect at lower frequencies. This is indeed correlated with the gradual reduction in conductivity as discussed below. The dielectric loss, otherwise referred to as tangent loss is a statistical measure of how much field is dissipated as heat in the process of polarization of a material by an applied field. The dielectric loss certainly decreases with frequency, and at higher frequencies, the loss angle is approximately the same because at higher frequency range nanoparticles expose a dispersive nature generated by multiple polarization effects [60]. In polar dielectrics, the orientations of molecules along the path of the applied electric field necessitate the utilization of sufficient electric energy to counteract the forces of internal friction. A portion of the electric energy is reserved for dipolar molecule rotations and other sorts of molecular transfer from one region to another, all of which entail energy losses. In nanophase materials, defects and space charge formation in the interphase layers activate an absorption current, culminating in a dielectric loss. Fig 11 (b) shows the dielectric loss of synthesized pure and zinc doped nickel oxide nanoparticles and it is evident that loss significantly decreases with an increase in dopant ratio. This tangent loss with doping proves the better electrical performance of doped nanoparticles in comparison with pure NiO nanoparticles. AC conductivity of nanoparticles with frequency-dependent function is plotted as shown in Fig 11 (c). The conductivity of a material is featured by the hopping mechanism and it relies on numbered parameters such as frequency of source signal, vacancy, and dopant concentration. It is related to dielectric loss as,

$$\sigma_{ac} = 2\pi f \varepsilon_0 \varepsilon_r \tan\delta \quad (34)$$

Due to the extreme potential barrier created by grain boundaries, charge carriers cannot relocate between grains, except for a very few charge carriers tunneling via this barrier and creating a slight but noticeable conductivity at low frequencies. Conductivity enhances as more charge carriers tunnel with accelerating frequency. Charge carriers gain adequate energy to overcome the potential barrier (resistive interfacial) over a certain frequency, resulting in a drastic increase in conductivity at higher frequencies. Dopant ions were observed to create defects in the NiO host system which seeks to isolate at grain boundaries [61]. Doping-induced defect ions contribute to the conception of a defect barrier across the grain boundary, obstructing the movement of charge carriers and lowering conductivity. Electronic properties Zn²⁺-doped NiO nanoparticles were estimated effectively which are directly dependent on the dielectric constant. The dielectric constant and its related properties of wide bandgap semiconductors are the objectives of Penn gap analysis which is determined by fitting the high-frequency dielectric constant with plasma energy [62]. The valence electron plasma energy is given by

$$\hbar\omega_p = 28.8 \left(\frac{Z\rho}{M} \right)^{1/2} \quad (35)$$

Where Z , ρ and M correspond to the total number of valence electrons, density, and molecular weight of as-synthesized nanoparticles. Penn gap and Fermi energy gap dependent on plasma energy are evaluated using the following expressions as,

$$E_p = \hbar\omega_p (\varepsilon_\infty - 1)^{-1/2} \quad (36)$$

$$E_F = 0.2948 (\hbar\omega_p)^{4/3} \quad (37)$$

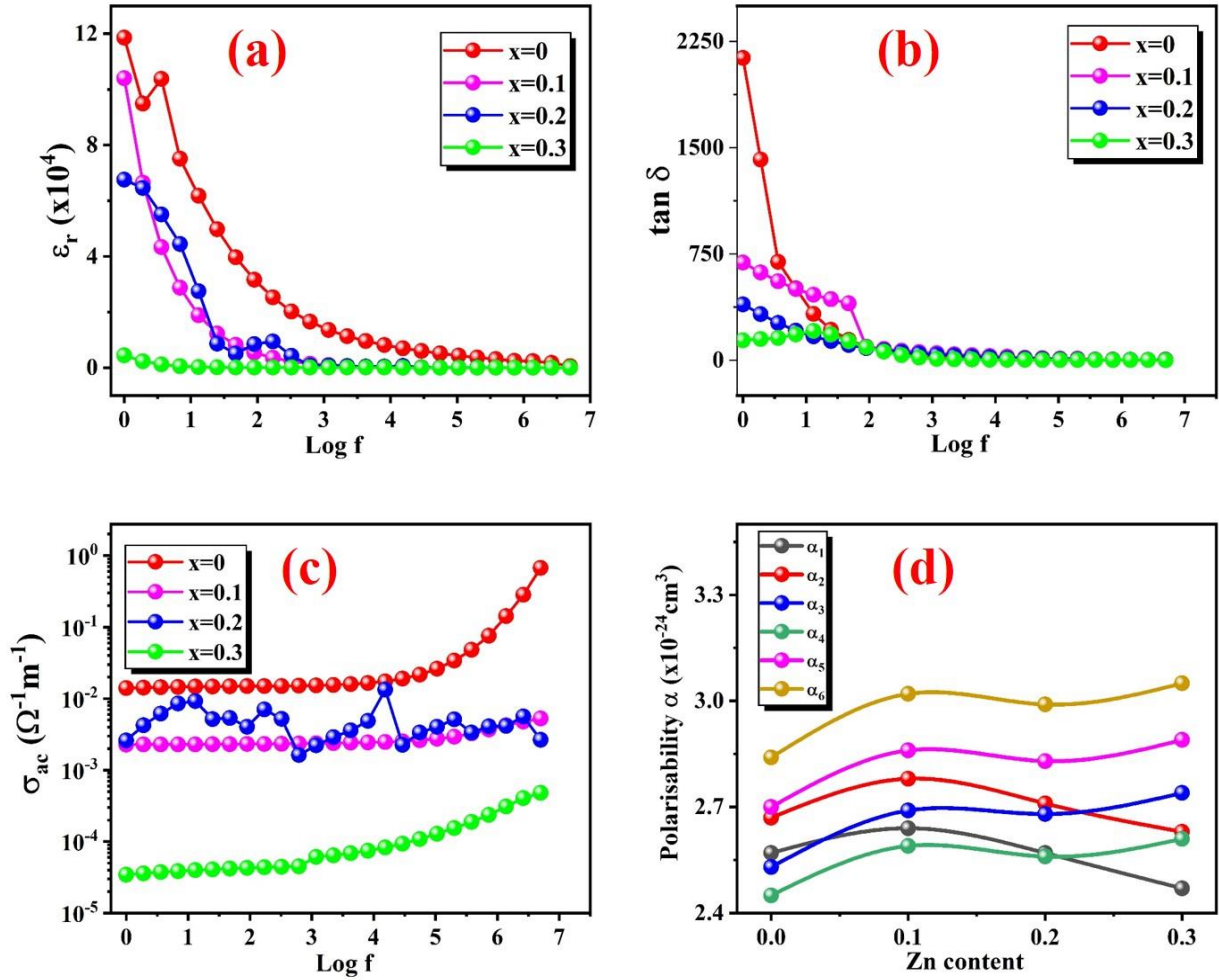


Fig 11. (a) Dielectric constant (b) tangent loss (c) AC conductivity Vs frequency dependent function (d) Polarizability Vs dopant variant

The relative affinity of a charge distribution, analogous to the electron cloud of an atom or molecule, and accordingly of any material body, to have its charges displaced by an applied electric field is referred to as electronic polarizability [63-64]. Different models were utilized to estimate the electronic polarizability (α) of nanoparticles and the quantities are tabulated in Table 4. According to the Penn model, α_1 was given as

$$\alpha_1 = \left[\frac{(\hbar\omega_p)^2 S_0}{(\hbar\omega_p)^2 S_0 + 3E_F^2} \right] \frac{M}{\rho} \times 0.396 \times 10^{-24} \quad (38)$$

Here S_0 is a constant and is given by

$$S_0 = 1 - \left[\frac{E_P}{4E_F} \right] + \frac{1}{3} \left[\frac{E_P}{4E_F} \right]^2 \quad (39)$$

Electronic polarizability (α_2) from Clausius-Mossotti relation is expressed as

$$\alpha_2 = \frac{3M}{4\pi N_a \rho} \left[\frac{\epsilon_\infty - 1}{\epsilon_\infty + 2} \right] \quad (40)$$

Lorentz-Lorenz equation proposes that for visible light $\epsilon' = n^2$, and so polarizability is related to refractive index as

$$\alpha_3 = \frac{3M}{4\pi N_a \rho} \left[\frac{n^2 - 1}{n^2 + 2} \right] \quad (41)$$

As polarizability is correlated with refractive index, it is also dependent on bandgap energy as

$$\alpha_4 = \left[1 - \frac{(E_g)^{1/2}}{4.06} \right] \frac{M}{\rho} \times 0.396 \times 10^{-24} \quad (42)$$

A systematic relationship existing between polarizability (α) and optical electronegativity ($\Delta\chi^*$) is calculated from the below expression as

$$\alpha_5 = \left[\frac{4.207+K}{7.207+K} \right] \frac{M}{\rho} \times 0.396 \times 10^{-24} \quad (43)$$

Here $K = \ln \Delta\chi^* (\ln \Delta\chi^* - 4.564)$ and $\Delta\chi^* = 0.2688 E_g$ for cubic systems.

Reddy et al. designed a relationship between polarizability (α) and bulk modulus (B) of synthesized nanoparticles as

$$\alpha_6 = \left[\frac{(5.563 - 0.033B)^2 - 1}{(5.563 - 0.033B)^2 + 2} \right] \frac{M}{\rho} \times 0.396 \times 10^{-24} \quad (44)$$

Where $B = 13.69 E_g + 46.90$.

Electronic polarizabilities estimated from six different relations are plotted versus the dopant concentration with nickel oxide nanoparticles in Fig 11 (d) and the quantities are relatively similar for all models.

Sn/Ni ratio	$\hbar\omega_p$ (eV)	E_F (eV)	E_P (eV)	Polarizability (10^{-24}cm^3)					
				α_1	α_2	α_3	α_4	α_5	α_6
0	25.60	22.24	10.40	2.57	2.67	2.53	2.45	2.70	2.84
0.1	24.58	21.06	10.65	2.64	2.78	2.69	2.59	2.86	3.02
0.2	24.52	21.00	11.05	2.57	2.71	2.68	2.56	2.83	2.99
0.3	24.19	20.63	11.73	2.47	2.63	2.74	2.61	2.89	3.05

Table 4. Electrical parameters of $\text{Zn}_x\text{Ni}_{1-x}\text{O}$ nanoparticles

3.6. BET Analysis

Porous framework and surface area characteristics of the synthesized pristine and Zn incorporated nickel oxide nanoparticles were inspected using BET analysis and the corresponding A-D isotherm curves were displayed in Fig 12 (a). It is evident that the surface area drastically increases from 15 to 54 m^2/g as the dopant concentration in NiO lattice also increases accordingly. The antibacterial and antifungal activity of doped samples are

discernibly affected by the porous structure of $Zn_xNi_{1-x}O$ nanoparticles. In addition, the high surface area generated is critical in technological applications such as energy retention and conversion circuits [65]. The A-D isotherm curve reflects type IV isotherm, which indicates the mesoporous structure as mentioned in the IUPAC classification as the absorbent pores are categorized into three groups: micropore (diameter < 2 nm), macropore (diameter > 50 nm), and mesopore (diameter 2–50 nm). Table 5 shows the estimated textural parameters and it is distinct that the synthesized nanoparticles are mesoporous in nature with relatively narrow pore distributions. Consequently, the small pore dimension, low pore volume, would endow the nanoparticles with good antimicrobial and robust mechanical attributes. The pore size distribution curve from the desorption branch of the isotherms was obtained using the Barrett-Joyner-Halenda (BJH) method, as illustrated in Fig 12 (b) and changes in the concentration of Zn content with surface area is shown in Fig 12 (c). The BET adsorption isotherm equation is given as [66],

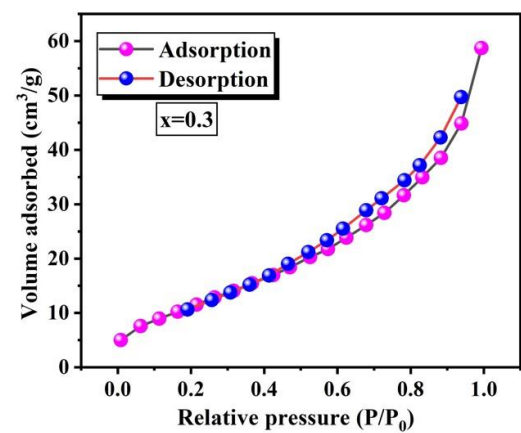
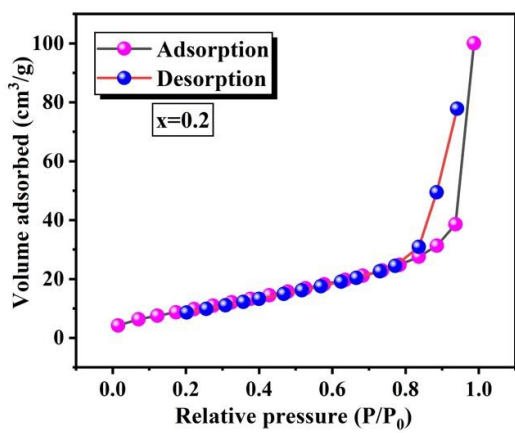
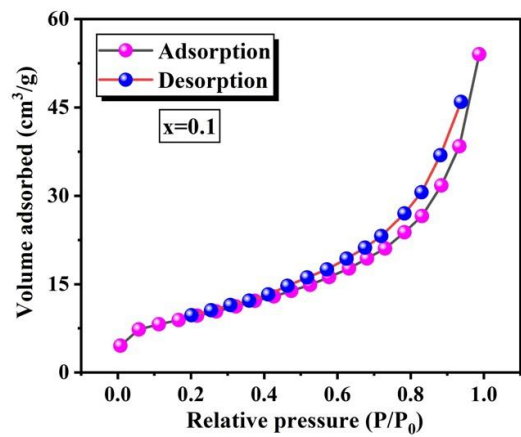
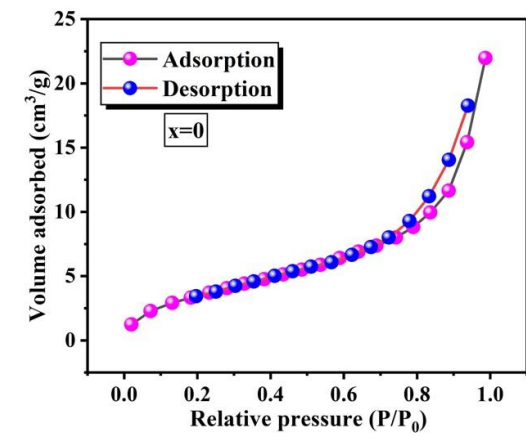
$$\frac{P/P_0}{V(1-P/P_0)} = \frac{C-1}{n_m C} (P/P_0) + \frac{1}{n_m C} \quad (45)$$

Where P and P_0 represents the partial and saturation vapor pressure of N_2 gas maintained at equilibrium given in pascal respectively; V is the nitrogen gas volume in mL adsorbed at Standard Temperature Pressure (STP); C and n_m denotes BET dimensionless constant and monolayer capacity related with the enthalpy of nitrogen gas adsorbed on porous materials. This $\frac{P/P_0}{V(1-P/P_0)}$ Vs. (P/P_0) linear plots form a straight line within the relative pressure ranging from 0.05 to 0.3 as displayed in Fig 12 (d). n_m is calculated from $\frac{1}{\text{slope} + \text{intercept}}$ and $\frac{\text{slope}}{\text{intercept}} + 1$ gives C from the linear plots. The specific surface area (a_s) is measured from the obtained parameters as,

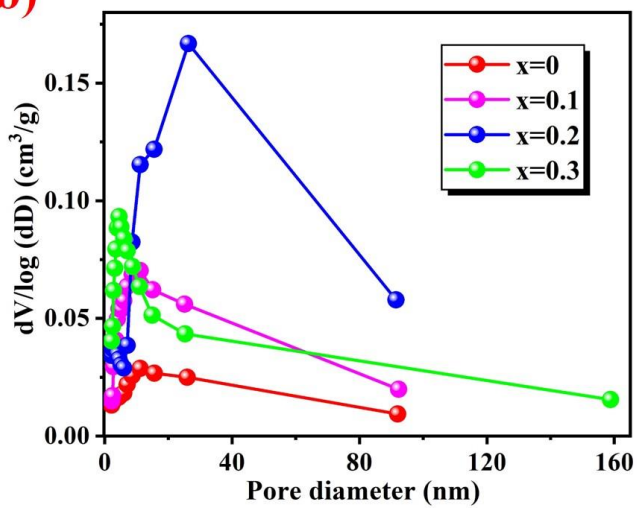
$$a_s = \frac{n_m L \sigma_m}{m \times 22400} \quad (46)$$

Where L denotes Avogadro constant ($6.023 \times 10^{23} \text{ mol}^{-1}$), σ_m equals to 16.2 \AA^2 and m is the molecular weight.

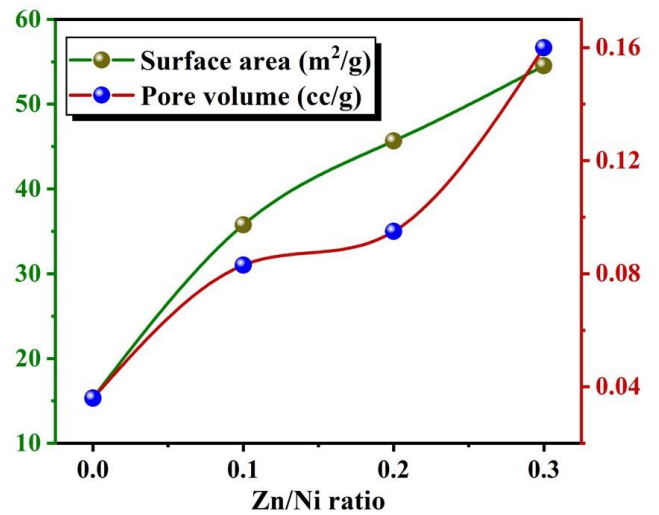
(a)



(b)



(c)



(d)

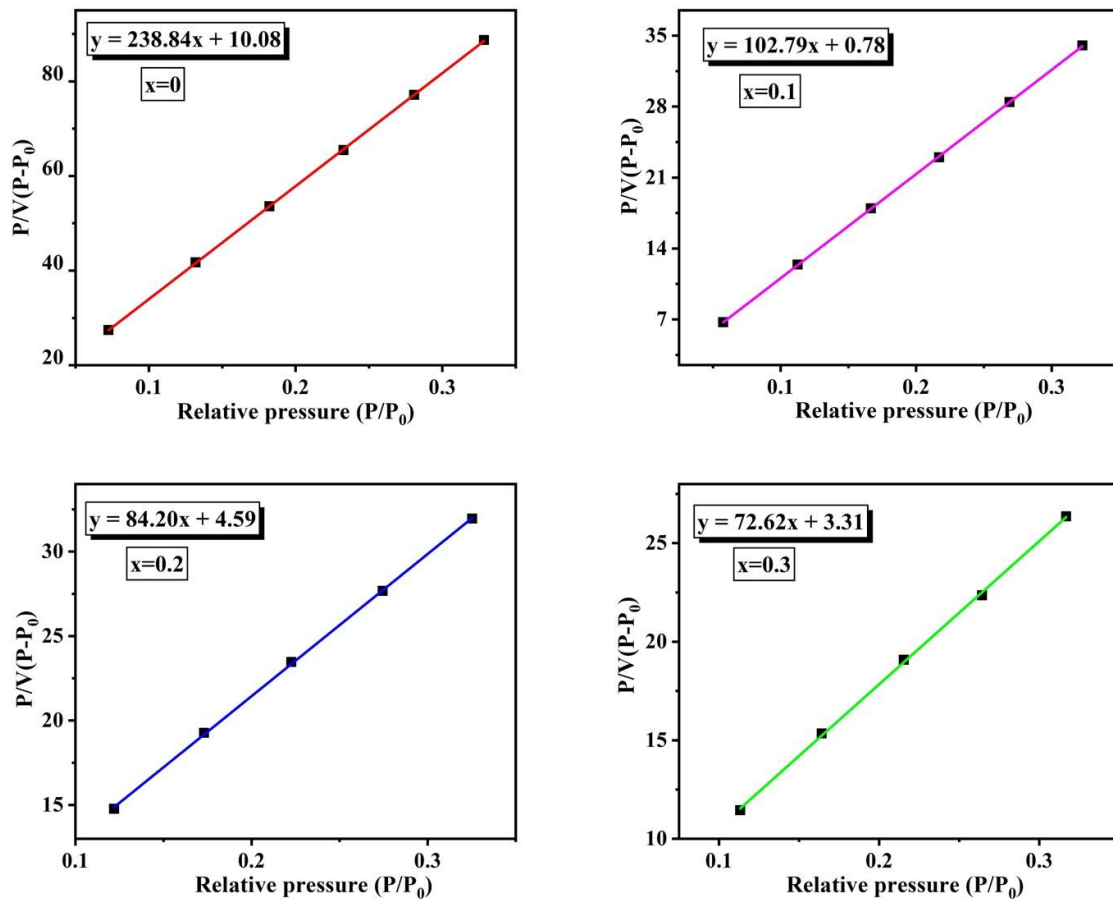


Fig 12. (a) N₂ Adsorption-Desorption isotherm curves (b) Pore size distribution from BJH plot (c) Plot of Sn/Ni ratio Vs. surface area (d) linear plot of A-D isotherms

Zn _x Ni _{1-x} O	Surface area (a) (m^2/g)	Pore diameter (nm)	Pore volume (cm^3/g)	Specific surface area (a_s) (m^2/g)
0	15.34	2.18	0.036	13.99
0.1	35.77	2.20	0.083	33.62
0.2	45.65	3.96	0.095	39.21
0.3	54.54	3.99	0.160	45.86

Table 5. Surface parameters calculated from BET analysis

3.6. Magnetic Properties

The magnetic response of undoped and Zn doped nanoparticles examined at room temperature was depicted in Fig 13 with different applied magnetic fields ranging from 0-20 kOe. Bulk nickel oxide in nature exhibits anti-ferromagnetism with Neel temperature (T_N) of ~523 K, controversially NiO at nano-scale realm reveals remarkable magnetic characteristics by showing ferromagnetism. The origination of ferromagnetic behaviour of synthesized

nanoparticles at room temperature is intricate to interpret and in addition, the prime reason for the samples to exhibit ferromagnetism is defects, which are most probably encountered at the surface and ultimately generated by the doping atoms where they are witnessed that oxygen-rich Zn²⁺ doped NiO nanoparticles are super paramagnetic but oxygen vacancies derivatives are ferromagnetic. Zinc doped nickel oxide ferromagnetism is intended to rise from the exchange interaction between dopant ions triggered by defects such as oxygen vacancy. Moreover, the interactions of localized electrons developed by oxygen vacancies cause the electrons to couple either in the spin-up or spin-down state. The Ni vacancies were found to induce the ferromagnetism in nickel sites with a spin orientation by polarizing the neighbouring ligand atoms of the vacancy potentially resulting in a collective localized magnetic moment explained by Bound Magnetic Polaron (BMP) theory [22, 67]. In a BMP mechanism for transition metal oxides, the defect originates from the oxygen vacancy which can capture one migrating electron and form a finite radius hydrogen-like orbit. The orbits overlap when the defects reach critical levels, forming a narrow impurity band. Thus the doped magnetic nickel ions within the radius coverage interact through the impurity band electrons and achieve ferromagnetism. The high surface-to-volume ratio formed by Zn doping results in the reduction in crystallite size which give rise to the distortion of surface atom and in turn to deformed surface atoms. These deformed surface atoms are responsible for the creation of oxygen vacancy defects, and the number of deformed atoms increases as crystallite size decreases, resulting in a reduction in saturation magnetization and an increase in coercivity. The magnetic properties and antimicrobial activity of synthesized nanoparticles are closely associated with each other. Smaller crystallite size accounts for the reduction in saturation magnetization which affects the microbial inhibition effect. Zinc doped NiO nanoparticles generate lesser M_s and so better antibacterial and antifungal response in comparison with pure nickel oxide nanoparticles [68]. The magnetic parametrics calculated from hysteresis loop are essential and also encounter various application in the domain of magnetic memory devices and spintronics which are summarized in Table 6. The diamagnetic nature of zinc doped with nickel atoms generate ferromagnetism and when Zn content increases from 10 to 30 %, the coercive nature of pure nanoparticles increases from 140-222 Oe. Fig 13 (b) shows the maximized image of the hysteresis loop. In addition, the magnetic structure may also transfer from multi-domain to single domain conformation as evidenced by the squareness ratio (M_r/M_s) inferred from the M-H loop (<1). Consequently, the magnetization cycle shifts from domain wall motion to magnetization rotation, prompting an enhancement in H_c . This pattern of response is witnessed in nanoparticles for the spinning moments in terms of energy barrier which is reliant on the surface area as $\Delta E = K_s S$ where S and K_s refers to the surface area of nanoparticles and surface anisotropy constant respectively. This phenomenon is accountable for an increase in coercivity as $H_c \sim \frac{1}{D}$ [69]. Fig 13 (c) presents the variation of saturation magnetization and coercivity with the zinc concentration in nickel oxide lattice.

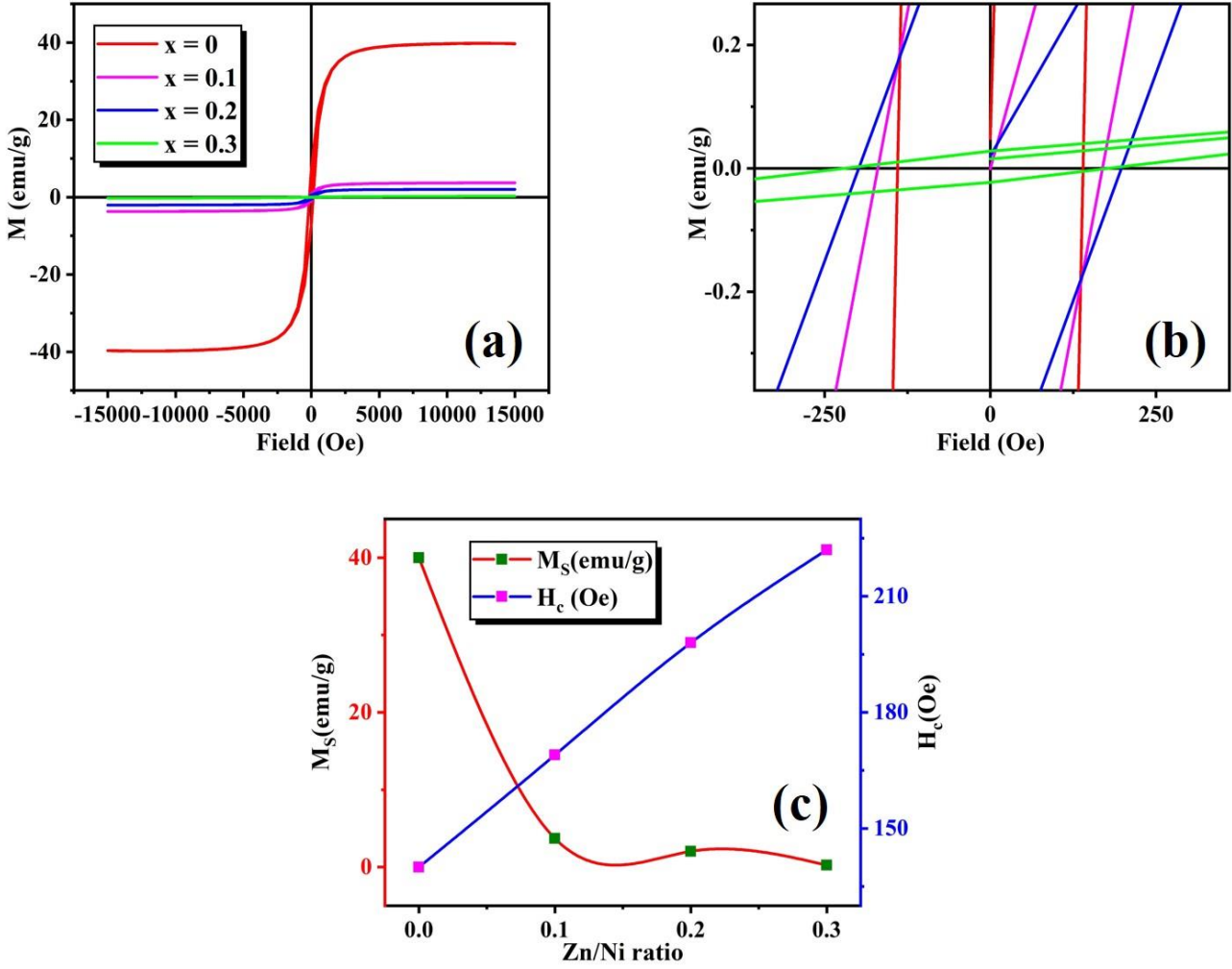


Fig 13. (a) M-H loop of Zn_xNi_{1-x}O nanoparticles (b) Maximized image of M-H loop (c) Variation of M_s and H_c with Zn content

"Law of Approach to Saturation (LAS)" model describes the dependence of magnetization M on the applied magnetic field for $H \gg H_c$ as [70],

$$M = M_s \left(1 - \frac{A}{H} - \frac{B}{H^2} \right) \chi H \quad (47)$$

Here, A and χ are parameters linked with the magnetic anisotropies dominant in nano-samples and paramagnetic susceptibility respectively. χH refers to the high field derivative of susceptibility functional only in high-temperature studies. Since the term $\frac{A}{H}$ does not add up to the computation, A becomes zero,

$$M = M_s \left(1 - \frac{B}{H^2} \right) \quad (48)$$

A linear fit may be used to derive the saturation magnetization from the intercept and magneto-crystalline anisotropy field from the slope, as illustrated in Fig 13 (d). The squareness ratio is smaller than 0.5, showing that nanoparticles interact via magnetostatic exchange and that the anisotropy constant decreases with doping. The parameters can be evaluated from the following expressions,

$$B = \frac{H_a}{15} \quad (49)$$

$$K_1 = \frac{M_s H_a}{2} \quad (50)$$

$$\mu_B = \frac{M \times M_s}{5585} \quad (51)$$

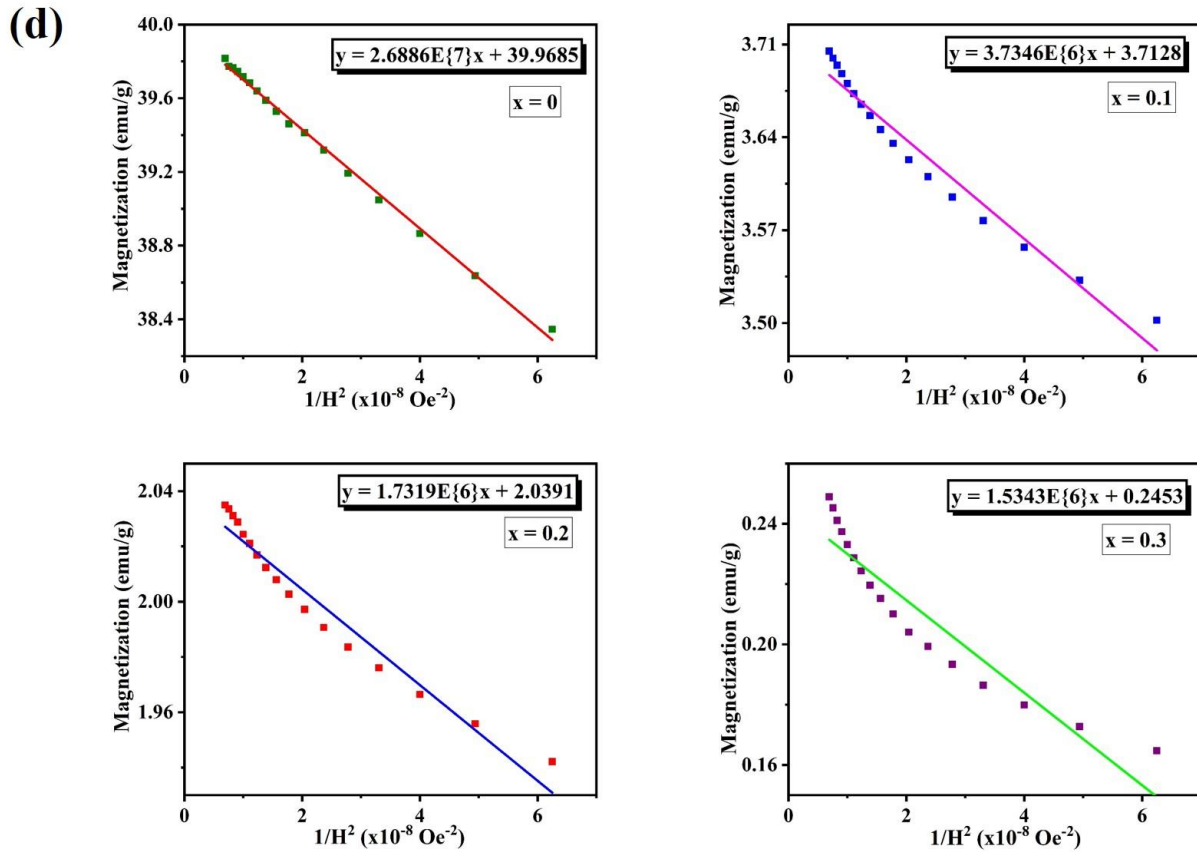


Fig 13 (d). LAS plot of pure and Zn incorporated nickel oxide nanoparticles

Zn/Ni ratio	H_c (Oe)	M_r (emu/g)	M_s (emu/g)	$\frac{M_r}{M_s}$	B ($10^7 Oe^2$)	H_a ($10^4 Oe$)	K_1 ($10^5 erg/cm^3$)	μ_B
0	140	1.14	39.96	0.02	2.68	2.00	4.013	0.534
0.1	169	0.96	3.71	0.25	0.37	0.74	0.138	0.050
0.2	198	0.58	2.03	0.28	0.17	0.50	0.051	0.027
0.3	222	0.02	0.24	0.08	0.15	0.47	0.005	0.003

Table 6. Magnetic parameters of $Zn_xNi_{1-x}O$ (x=0, 0.1, 0.2, 0.3) nanoparticles

3.7. Antibacterial and Antifungal activity

Antibacterial and antifungal activity of pristine and Zn doped NiO nanoparticles synthesized via the chemical method was tested against different gram positive, gram negative bacterial pathogens, and fungal strains as displayed in Fig 14 (a-f) and it is apparent from the graph (Fig 14 (g)) that the activity is comparatively higher in gram-negative bacteria (*E. coli*, *K. pneumonia*) than in gram-positive bacteria (*E. faecalis*, *S. aureus*) as gram-negative bacteria possess a thin cell wall with a single layer of peptidoglycan which is more susceptible to damage, whereas Gram-positive bacteria have thick multiple layers of peptidoglycan. Furthermore, a notable effect was spotted against *Aspergillus niger* (17mm) and *Escherichia coli* (17 mm). Conventionally, the sample has increased antimicrobial activity if the Zone Of Inhibition (ZOI) is wider than 6 mm. The inhibition zones (mm) when bacteria and fungi were treated with 100 µg/ml of NiO and nickel oxide doped with different concentrations of zinc samples are presented in Fig 14 (a-f) and it is certain that the synthesized nanoparticles exhibit potent activity against the microbes. The robust activity can be detected in the highly doped samples where N1, N2, N3, N4, e, and f correspond to $x=0$, 0.1, 0.2, 0.3, negative control (DMSO), and positive control (Azithromycin for bacteria and Clotrimazole for fungi) respectively. $Zn_{1-x}Ni_xO$ ($x=0.3$) exhibited better antimicrobial activity than other concentrations signifying that it allows for a higher active surface and greater oxygen vacancies. The improved antibacterial action is attributed to the smaller crystallite size of doped NiO nanoparticles, which boosts dispersibility and allows for the inference of extracellular Ni^{2+} with intracellular Ca^{2+} metabolism, resulting in cell injury. Bactericidal activity of such nanoparticles is also impacted by the crystallite size, concentration of nanoparticles dispersed, and stability of particles in the growth medium [71-72]. The antimicrobial mechanism exhibited by zinc doped NiO nanoparticles also depends on the degree of susceptibility of microbes. When the nanoparticles come into contact with the microbe, they form an electrical bond with the microbial surface. Their much reduced size aids entrance into the bacterial cell via trans membrane proteins and proton motive force effect. It has a greater affinity towards sulfur groups existing in proteins to produce thiols and phosphates creating complexes that cause DNA damage. The interaction of NPs with cysteine residues causes the production of ROS by blocking electrons at terminal oxidase, resulting in microbial cell death.

The dissociation of excess carboxylic groups at the surface of the microbial cell is responsible for the global charge of the bacterial cell to be negative at physiological pH and NiO particles carrying a positive surface charge get electrostatically bonded to the negative cell surface, inhibiting cell activity. Some studies report that the reduced size of nanoparticles is a major factor in penetrating the microbial cell membrane. The outer cell membranes of synthesized nanoparticles have pores in the nanometer range, and that nanoparticles with diameters smaller than the pores can permeate the cell membrane eventually resulting in uncontrolled mass transmission across the membranes. The mechanism for the antimicrobial activity of pure and zinc doped nickel oxide nanoparticles can be associated with a number of aspects, including: (1) the accumulation of nanoparticles on the surface of the microbe, which provokes the cell envelope to be destroyed and intracellular components to be released (2) the formation of Ni ions and their electrostatic interaction with the bacterial cell wall. This contact increases nanoparticle penetration through the cell membrane, causing

damage to bacterial cellular constituents (3) the formation of Reactive Oxygen Species (ROS), which have the potential to impair DNA and proteins, ultimately leading to microbial death [73-74]. Superoxide and hydroxyl radicals, which are formed by metal-oxide nanoparticles are two ROS that damage cells. ROS oxidize double bonds in phospholipids, increasing membrane fluidity that make cells highly susceptible to osmotic stress. Iron-sulphur complexes which serve as cofactors in enzymes can also be destroyed by ROS.

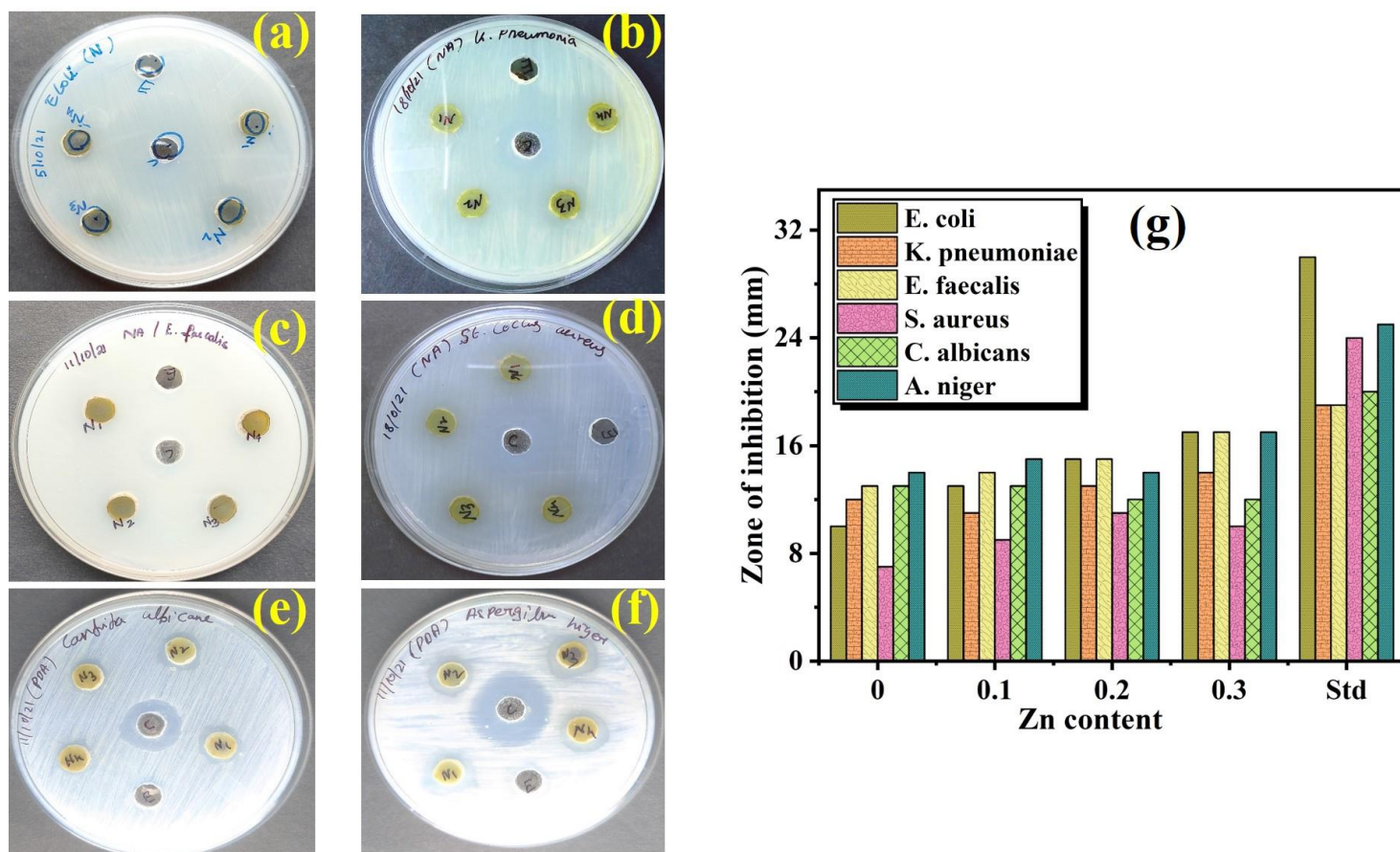


Fig 14. ZOI of (a) E. coli (b) K. pneumoniae (c) E. faecalis (d) S. aureus (e) C. albicans and (f) A. niger (g) Variation of antimicrobial activity with Zn content

The schematic representation for the formation of ROS by synthesized nanoparticles and damage caused to the microbial cell by ROS is depicted in Fig 15. When light strikes NiO nanomaterial with a photon energy greater than the band gap energy E_g , photoexcitation causes holes (h^+) to develop in the valence band and electrons (e^-) to generate in the conduction band. These photo-excited carriers, which have intense oxidizing and reducing characteristics, combined with the donor (H_2O and OH ions) and acceptor (O_2) further resulting in the proliferation of different reactive oxygen species. The excited electron attaches to the molecular oxygen to create the superoxide anion ($O_2^{\cdot-}$) which subsequently reacts with free water molecules to render rigorous hydrogen peroxide (H_2O_2). The holes grab electrons from water and hydroxyl ions, yielding hydroxyl radicals ($\cdot OH$) that damage the cell membrane, DNA, and proteins. Since the toxicity activity and stability of zinc doped

nanoparticles are effective, they could be credibly engage in antimicrobial coatings that are extremely beneficial in environmental and biomedical applications. E. coli bacteria can cause severe anaemia, diarrhoea, abdominal pain, and sometimes renal failure, while gram-positive E. faecalis bacterium has a negative impact on the digestive tract. S. aureus and K. pneumonia bacteria produce severe infections in humans, such as pneumonia and bloodstream infection in the respiratory (breathing) tract. In addition, C. albicans is a human pathogen that causes skin infections in the tongue and nails, which are more chronic in those with weakened immune systems. A. niger usually affects the respiratory system in humans and as a result, pure and Zn²⁺doped NiO nanoparticles that have been expertly prepared by a sol-gel process can be used to treat bloodstream infection, kidney failure, digestive problems, skin epidemics, pneumonia, respiratory dilemmas, and urinary tract infections. Nanomaterials are of immense importance in food technology by virtue of their high reactivity, optimized bioavailability and bioactivity, and unique surface features [75]. The antimicrobial capabilities of NiO nanoparticles against foodborne pathogens have elevated their usage in food packaging, and they might potentially be implemented in food nanotechnology.

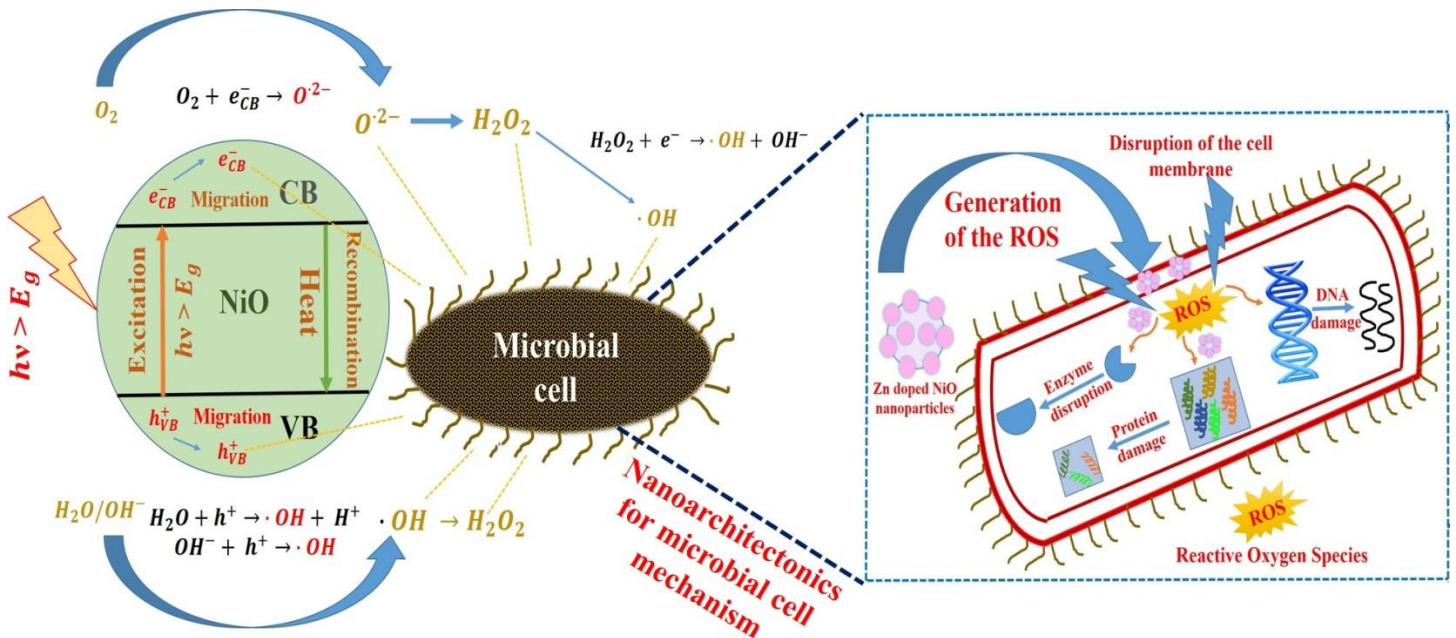


Fig 15. Schematic representation of the light irradiated Zn doped NiO nanoparticles and the production of ROS stimulating bacterial death

4. Conclusion

Pure and zinc doped nickel oxide nanoparticles ($Zn_xNi_{1-x}O$) with a sequence of dopant concentrations at $x=0, 0.1, 0.2$ and 0.3 M were successfully synthesized via a simple sol-gel approach availing citric acid as a congealing agent. The Zn substitution on NiO lattice resulted in a substantial discrepancy in structural, optical, magneto-electrical, and antimicrobial properties to a significant extent. The face-centered cubic configuration of as-synthesized nanoparticles was confirmed from XRD analysis and the respective crystallite size estimated from the Scherrer model decreases from 28.94 to 7.15 nm with a significant augmentation in the dopant content. The structural morphology of prepared NiO nanoparticles

from SEM contours the porous spherical conformation and the particle size (73-41 nm) enumerated with the histogram images is in congruence with crystallite size calculated from XRD data. The presence of zinc in nickel oxide lattice with the compositional percentage of respective elements was further confirmed from EDX spectra. FTIR spectra affirm the corresponding vibrational frequencies of nanoparticles and the bond length measured from force constant decreases with zinc content which is in accordance with the blue shift observed from the optical absorption. The optical studies revealed the advancement in band gap energy (blue shift) corresponding to the Burstein Moss shift phenomenon and other fundamental optical parameters such as refractive index calculated from five different models and electronegativity of pure and doped samples were evaluated. Dispersion parametric associated with the optical and energy criterion which is derived from the WDD approach play a pivotal part in the design of opto-electronic and non-linear optical devices. Urbach energy of the synthesized nanoparticles manifests the prominent disorders existing in the zinc doped samples and it showcases an increasing trend from 0.67 to 8.74 eV, proving that density of defect states rises with dopant ratio. Electrical properties like dielectric constant, loss and AC conductivity of synthesized nanoparticles were explored conducive to compute plasma energy, Penn and Fermi gap in compliance with Maxwell-Wagner and Koop's theory. The surface area was found to be increasing from 15 to 54 m²/g with zinc concentration as estimated from BET analysis. The pore size distribution such as pore diameter and volume of as-synthesized samples were evaluated from the BJH model and also affirms the mesoporous nature of the NiO nanoparticles. The significant increase in active surface area and the reduction in particle size drastically influence the antibacterial and antifungal activity. The insertion of zinc atoms in nickel oxide lattice generates the ferromagnetic behavior and the highest coercivity (222 Oe) is observed with the declination in saturation magnetization (0.24 emu/g) from the highest dopant ratio $x=0.3$. In addition, the effective antibacterial and antifungal response exhibited by undoped and Zn incorporated nickel oxide nanoparticles were discussed for the mass production of antimicrobial agents and its inevitable usage in agricultural sectors.

Acknowledgments

The authors are grateful to the management of Loyola College (Autonomous), Chennai 600 034 for awarding the Loyola College-Times of India project (3LCTOI14PHY002) for providing fundamental facilities for the synthesis of nanoparticles. The authors extend their gratitude to Dr. C. Justin Raj, Department of Chemistry, Dongguk University-Seoul Campus, Jung-gu, Seoul, 04620, Republic of Korea for his valuable insights. We acknowledge Nanotechnology Research Centre (NRC), SRMIST for granting the characterization facilities for XRD, UV-VIS, VSM studies.

Declaration of Interest

The authors declare that they have no known competing financial interests or personal relationships that could have appeared to influence the work reported in this paper. We wish to confirm that there are no known conflicts of interest among all the authors.

References

1. M. Aftab, M. Z. Butt, D. Ali, Z. H. Aftab, M. U. Tanveer, B. Fayyaz, Investigation of antifungal response of NiO and copper-doped NiO thin films against *Aspergillus niger* and *Macrophomina phaseolina* fungi. *Environmental Science and Pollution Research*.1-13 (2021)
2. A. A. Mohamed, M. Abu-Elghait, N. E. Ahmed, S. S. Salem, Eco-friendly mycogenic synthesis of ZnO and CuO nanoparticles for in vitro antibacterial, antibiofilm, and antifungal applications. *Biological trace element research*. 199(7), 2788-2799 (2021)
3. K. Rambabu, G. Bharath, F. Banat, P. L. Show, Green synthesis of zinc oxide nanoparticles using *Phoenix dactylifera* waste as bioreductant for effective dye degradation and antibacterial performance in wastewater treatment. *Journal of hazardous materials*. 402, 123560 (2021)
4. K. Atacan, N. Güy, M. Ozmen, M. Özacar, Fabrication of silver doped different metal oxide nanoparticles and evaluation of their antibacterial and catalytic applications. *Applied Surface Science Advances*. 6, 100156 (2021)
5. S. M. Savassa, N. M. Duran, E. S. Rodrigues, E. De Almeida, C. A. Van Gestel, T. F. Bompadre, P. H. W. de Carvalho, Effects of ZnO nanoparticles on *Phaseolus vulgaris* germination and seedling development determined by X-ray spectroscopy. *ACS Applied Nano Materials*. 1(11), 6414-6426 (2018)
6. F. Maglangit, Y. Yu, H. Deng, Bacterial pathogens: threat or treat (a review on bioactive natural products from bacterial pathogens). *Natural Product Reports*. 38(4), 782-821 (2021)
7. S. Marot, I. Malet, V. Leducq, K. Zafilaza, D. Sterlin, D. Planas, A. Gothland, A. Jary, K. Dorgham, T. Bruel, S. Burrel, Rapid decline of neutralizing antibodies against SARS-CoV-2 among infected healthcare workers. *Nature communications*. 12(1), 1-7 (2021)
8. P. A. Sheena, H. Hitha, A. Sreedevi, T. Varghese, Microstructural characterization and modified spectral response of cobalt doped NiO nanoparticles. *Materials Chemistry and Physics*, 229, 412-420 (2019)
9. J. Moavi, F. Buazar, M. H. Sayahi, Algal magnetic nickel oxide nanocatalyst in accelerated synthesis of pyridopyrimidine derivatives. *Scientific reports*. 11(1), 1-14 (2021)
10. A. C. Nwanya, M. M. Ndipingwi, C. O. Ikpo, R. M. Obodo, S. C. Nwanya, S. Botha, F. I. Ezema, E. I. Iwuoha, M. Maaza, Zea mays lea silk extract mediated synthesis of nickel oxide nanoparticles as positive electrode material for asymmetric supercapattery. *Journal of Alloys and Compounds*. 822, 153581 (2020)
11. G. V. Williams, J. Kennedy, P. P. Murmu, S. Rubanov, S. V. Chong, The effect of different Fe concentrations on the structural and magnetic properties of near surface superparamagnetic Ni_{1-x}Fe_x nanoparticles in SiO₂ made by dual low energy ion implantation. *Journal of Magnetism and Magnetic Materials*. 473, 125-130 (2019)
12. C. J. Raj, R. Manikandan, K. H. Yu, G. Nagaraju, M. S. Park, D. W. Kim, S. Y. Park, B. C. Kim, Engineering thermally activated NiMoO₄ nanoflowers and biowaste derived activated carbon-based electrodes for high-performance supercapatteries. *Inorganic Chemistry Frontiers*. 7(2), 369-384 (2020)
13. M. Chhetri, C. N. R. Rao, Photoelectrochemical hydrogen generation employing a Cu₂O-based photocathode with improved stability and activity by using Ni_xP_y as the cocatalyst. *Physical Chemistry Chemical Physics*. 20(22), 15300-15306 (2018)
14. R. Manikandan, C. J. Raj, K. H. Yu, B. C. Kim, Self-coupled nickel sulfide@ nickel vanadium sulfide nanostructure as a novel high capacity electrode material for supercapattery. *Applied Surface Science*. 497, 143778 (2019)
15. S. C. Chen, T. Y. Kuo, H. C. Lin, R. Z. Chen, H. Sun, Optoelectronic properties of p-type NiO films deposited by direct current magnetron sputtering versus high power impulse magnetron sputtering. *Applied Surface Science*, 508, 145106 (2020)
16. N. A. Mala, S. Sivakumar, K. M. Batoo, M. Hadi, Design and fabrication of iron-doped nickel oxide-based flexible electrode for high-performance energy storage applications. *Inorganic Chemistry Communications*. 131, 108797 (2021)

17. A. A. Ezhilarasi, J. J. Vijaya, L. J. Kennedy, K. Kaviyarasu, Green mediated NiO nano-rods using Phoenix dactylifera (Dates) extract for biomedical and environmental applications. *Materials Chemistry and Physics*. 241, 122419 (2020)
18. I. D. Likasari, R. W. Astuti, A. Yahya, N. Isnaini, G. Purwiandono, H. Hidayat, W. P. Wicaksono, I. Fatimah, NiO nanoparticles synthesized by using Tagetes erecta L leaf extract and their activities for photocatalysis, electrochemical sensing, and antibacterial features. *Chemical Physics Letters*. 780, 138914 (2021)
19. I. Kumar, B. Yaseen, C. Gangwar, S. K. Mishra, R. M. Naik, Environmental benign synthesis and characterization of nickel oxide nanoparticles using chicken egg white as template and evaluations of their antibacterial/antifungal activities. *Materials Today: Proceedings*. 46, 2272-2276 (2021)
20. S. Ghazal, A. Akbari, H. A. Hosseini, Z. Sabouri, F. Forouzanfar, M. Khatami, M. Darroudi, Sol-gel biosynthesis of nickel oxide nanoparticles using Cydonia oblonga extract and evaluation of their cytotoxicity and photocatalytic activities. *Journal of Molecular Structure*. 1217, 128378 (2020)
21. R. Nallendran, G. Selvan, A. R. Balu, NiO coupled CdO nanoparticles with enhanced magnetic and antifungal Properties. *Surfaces and Interfaces*, 15, 11-18 (2019)
22. B. Kisan, J. Kumar, P. Alagarsamy, Room temperature ferromagnetism in Zn-doped NiO nanoparticles: An experimental and DFT+ U approach. *Journal of Alloys and Compounds*. 868, 159176 (2021)
23. N. D. Cuong, P. L. Quang, N. T. N. Anh, D. T. Quang, P. C. Nam, K. Q. Trung, S. T. Nguyen, N. Van Hieu, Facile post-synthesis and gas sensing properties of highly porous NiO microspheres. *Sensors and Actuators A: Physical*. 296, 110-120 (2019)
24. H. Wang, H. Yuan, J. Yu, C. Zhang, K. Li, M. You, W. Li, J. Shao, J. Wei, X. Zhang, R. Chen, Boosting the Efficiency of NiO_x-Based Perovskite Light-Emitting Diodes by Interface Engineering. *ACS Applied Materials & Interfaces*. 12(47), 53528-53536 (2020)
25. T. U. D. Thi, T. T. Nguyen, Y. D. Thi, K. H. T. Thi, B. T. Phan, K. N. Pham, Green synthesis of ZnO nanoparticles using orange fruit peel extract for antibacterial activities. *RSC Advances*. 10(40), 23899-23907 (2020)
26. A. S. Bhosale, K. K. Abitkar, P. S. Sadalage, K. D. Pawar, K. M. Garadkar, Photocatalytic and antibacterial activities of ZnO nanoparticles synthesized by chemical method. *Journal of Materials Science: Materials in Electronics*. 32(15), 20510-20524 (2021)
27. R. Perveen, S. Shujaat, Z. Qureshi, S. Nawaz, M. I. Khan, M. Iqbal, Green versus sol-gel synthesis of ZnO nanoparticles and antimicrobial activity evaluation against panel of pathogens. *Journal of Materials Research and Technology*. 9(4), 7817-7827 (2020)
28. M. A. Subhan, T. Ahmed, N. Uddin, A. K. Azad, K. Begum, Synthesis, characterization, PL properties, photocatalytic and antibacterial activities of nano multi-metal oxide NiO. CeO₂. ZnO. *Spectrochimica Acta Part A: Molecular and Biomolecular Spectroscopy*, 136, 824-831 (2015)
29. A. F. Fathima, R. J. Mani, K. Sakthipandi, K. Manimala, A. Hossain, Enhanced antifungal activity of pure and iron-doped ZnO nanoparticles prepared in the absence of reducing agents. *Journal of Inorganic and Organometallic Polymers and Materials*. 30(7), 2397-2405 (2020)
30. Y. W. Baek, Y. J. An, Microbial toxicity of metal oxide nanoparticles (CuO, NiO, ZnO, and Sb₂O₃) to Escherichia coli, Bacillus subtilis, and Streptococcus aureus. *Science of the total environment*. 409(8), 1603-1608 (2011)
31. M. S. Kumar, T. L. Soundarya, G. Nagaraju, G. K. Raghu, N. D. Rekha, F. A. Alharthi, B. Nirmala, Multifunctional applications of Nickel oxide (NiO) nanoparticles synthesized by facile green combustion method using Limonia acidissima natural fruit juice. *Inorganica Chimica Acta*. 515, 120059 (2021)
32. T. S. Aldeen, H. E. A. Mohamed, M. Maaza, ZnO nanoparticles prepared via a green synthesis approach: Physical properties, photocatalytic and antibacterial activity. *Journal of Physics and Chemistry of Solids*. 160, 110313 (2022)
33. N. Joseph, P. M. Shafi, J. S. Sethulakshmi, R. Karthik, A. C. Bose, J. J. Shim, Three dimensional NiO nanonetwork electrode for efficient electrochemical energy storage application. *Electrochimica Acta*. 399, 139392 (2021)

34. G. K. Williamson, R. E. Smallman, Dislocation densities in some annealed and cold-worked metals from measurements on the X-ray debye-scherrer spectrum. *Philosophical magazine*. 1(1), 34-46 (1956)
35. K. Singh, A. Thakur, A. Awasthi, A. Kumar, Structural, morphological and temperature-dependent electrical properties of BN/NiO nanocomposites. *Journal of Materials Science: Materials in Electronics*. 31(16), 13158-13166 (2020)
36. S. Yousaf, S. Zulfiqar, M. N. Shahi, M. F. Warsi, N. F. Al-Khali, M. F. A. Aboud, I. Shakir, Tuning the structural, optical and electrical properties of NiO nanoparticles prepared by wet chemical route. *Ceramics International*, 46(3), 3750-3758 (2020)
37. M. N. Siddique, A. Ahmed, P. Tripathi, Enhanced optical properties of pure and Sr doped NiO nanostructures: A comprehensive study. *Optik*. 185, 599-608 (2019)
38. H. A. Ariyanta, T. A. Ivandini, Y. Yulizar, Novel NiO nanoparticles via phytosynthesis method: Structural, morphological and optical properties. *Journal of Molecular Structure*. 1227, 129543 (2021)
39. N. J. Usharani, S. S. Bhattacharya, Effect of defect states in the optical and magnetic properties of nanocrystalline NiO synthesised in a single step by an aerosol process. *Ceramics International*. 46(5), 5671-5680 (2020)
40. M. H. Mamat, N. Parimon, A. S. Ismail, I. S. Banu, S. S. Basha, R. A. Rani, A. S. Zoolfakar, M. F. Malek, A. B. Suriani, M. K. Ahmad, M. Rusop, Synthesis, structural and optical properties of mesostructured, X-doped NiO (x= Zn, Sn, Fe) nanoflake network films. *Materials Research Bulletin*. 127, 110860 (2020)
41. P. Gupta, N. K. Pandey, K. Kumar, B. C. Yadav, Structural, optical and LPG sensing properties of zinc-doped nickel oxide pellets operated at room temperature. *Sensors and Actuators A: Physical*. 319, 112484 (2021)
42. J. Tauc, R. Grigorovici, A. Vancu, Optical properties and electronic structure of amorphous germanium. *physica status solidi (b)*, 15(2), 627-637 (1966)
43. P. R. Jubu, F. K. Yam, V. M. Igba, K. P. Beh, Tauc-plot scale and extrapolation effect on bandgap estimation from UV-vis-NIR data—a case study of β -Ga₂O₃. *Journal of Solid State Chemistry*. 290, 121576 (2020)
44. M. H. Babu, J. Podder, B. C. Dev, M. Sharmin, p to n-type transition with wide blue shift optical band gap of spray synthesized Cd doped CuO thin films for optoelectronic device applications. *Surfaces and interfaces*. 19, 100459 (2020)
45. R. E. Marotti, P. Giorgi, G. Machado, E. A. Dalchiele, Crystallite size dependence of band gap energy for electrodeposited ZnO grown at different temperatures. *Solar Energy Materials and Solar Cells*. 90(15), 2356-2361 (2006)
46. D. J. Borah, A. T. T. Mostako, Investigation on dispersion parameters of Molybdenum Oxide thin films via Wemple–DiDomenico (WDD) single oscillator model. *Applied Physics A*. 126(10), 1-13 (2020)
47. I. M. El Radaf, Dispersion parameters, linear and nonlinear optical analysis of the SnSb₂S₄ thin films. *Applied Physics A*. 126(5), 1-10 (2020)
48. T. A. Taha, N. Hendawy, S. El-Rabaie, A. Esmat, M. K. El-Mansy, Effect of NiO NPs doping on the structure and optical properties of PVC polymer films. *Polymer Bulletin*. 76(9), 4769-4784 (2019)
49. T. Munawar, F. Iqbal, S. Yasmeen, K. Mahmood, A. Hussain, Multi metal oxide NiO-CdO-ZnO nanocomposite—synthesis, structural, optical, electrical properties and enhanced sunlight driven photocatalytic activity. *Ceramics International*. 46(2), 2421-2437 (2020)
50. Z. R. Khan, K. V. Chandekar, A. Khan, N. Akhter, M. A. Sayed, M. Shkir, H. Algarni, S. AlFaify, An impact of novel Terbium (Tb) doping on key opto-nonlinear optical characteristics of spray pyrolyzed NiO nanostructured films for opto-nonlinear applications. *Materials Science in Semiconductor Processing*. 138, 106260 (2022)
51. S. H. Wemple, M. DiDomenico Jr, Behavior of the electronic dielectric constant in covalent and ionic materials. *Physical Review B*. 3(4), 1338 (1971)
52. A. A. Al-Ghamdi, W. E. Mahmoud, S. J. Yaghmour, F. M. Al-Marzouki, Structure and optical properties of nanocrystalline NiO thin film synthesized by sol-gel spin-coating method. *Journal of Alloys and compounds*. 486(1-2), 9-13 (2009)

53. K. Kumar, V. C. Vincent, G. Bakiyaraj, K. Kirubavathi, K. Selvaraju, Investigations of solid state, optical, NLO, dielectric and mechanical behaviour of Methyl para-Hydroxybenzoate crystal. *Optik*. 226, 165738 (2021)
54. M. M. El-Nahass, M. Emam-Ismail, M. El-Hagary, Structural, optical and dispersion energy parameters of nickel oxide nanocrystalline thin films prepared by electron beam deposition technique. *Journal of Alloys and Compounds*. 646, 937-945 (2015)
55. V. Ganesh, L. Haritha, M. A. Manthrammel, M. Shkir, S. AlFaify, An impact of La doping content on physical properties of NiO films facilely casted through spin-coater for optoelectronics. *Physica B: Condensed Matter*. 582, 411955 (2020)
56. M. Rashad, A. A. A. Darwish, S. I. Qashou, K. F. Abd El-Rahman, Influence of ultraviolet irradiation on physical properties of nano-NiO films for optical applications. *Applied Physics A*. 126(11), 1-9 (2020)
57. S. John, C. Soukoulis, M. H. Cohen, E. N. Economou, Theory of electron band tails and the Urbach optical-absorption edge. *Physical review letters*. 57(14), 1777 (1986)
58. M. Zahan, J. Podder, Surface morphology, optical properties and Urbach tail of spray deposited Co_3O_4 thin films. *Journal of Materials Science: Materials in Electronics*. 30(4), 4259-4269 (2019)
59. A. Sakthisabarimoorathi, S. M. B. Dhas, M. Jose, Fabrication of monodispersed $\alpha\text{-Fe}_2\text{O}_3@ \text{SiO}_2$ core-shell nanospheres and investigation of their dielectric behavior. *Journal of Alloys and Compounds*. 771, 1-8 (2019)
60. N. Giri, A. Mondal, S. Sarkar, R. Ray, Doping-induced dielectric and transport properties of $\text{Ni}_{1-x}\text{Zn}_x\text{O}$. *Journal of Materials Science: Materials in Electronics*. 31(15), 12628-12637 (2020)
61. C. Belkhaoui, N. Mzabi, H. Smaoui, Investigations on structural, optical and dielectric properties of Mn doped ZnO nanoparticles synthesized by co-precipitation method. *Materials Research Bulletin*. 111, 70-79 (2019)
62. S. Krishnan, C. J. Raj, R. Robert, A. Ramanand, S. J. Das, Mechanical, theoretical and dielectric studies on ferroelectric lithium ammonium sulphate (LAS) single crystals. *Solid-state electronics*. 52(8), 1157-1161 (2008)
63. S. Kalyanaraman, P. M. Shajinshinu, S. Vijayalakshmi, Refractive index, band gap energy, dielectric constant and polarizability calculations of ferroelectric Ethylenediaminium Tetrachlorozincate crystal. *Journal of Physics and Chemistry of Solids*. 86, 108-113 (2015)
64. R. R. Reddy, K. R. Gopal, K. Narasimhulu, L. S. S. Reddy, K. R. Kumar, G. Balakrishnaiah, M. R. Kumar, Interrelationship between structural, optical, electronic and elastic properties of materials. *Journal of alloys and compounds*. 473(1-2), 28-35 (2009)
65. S. Pordel, M. Rabbani, R. Rahimi, M. Heidari-Golafzani, A. Azad, Synthesis of mesoporous $\text{NiO}/\text{Bi}_2\text{WO}_6$ nanocomposite for selective oxidation of alcohols. *Solid State Sciences*. 107, 106306 (2020)
66. F. Motahari, M. R. Mozdianfard, F. Soofivand, M. Salavati-Niasari, NiO nanostructures: synthesis, characterization and photocatalyst application in dye wastewater treatment. *Rsc Advances*, 4(53), 27654-27660 (2014)
67. M. N. Siddique, P. Tripathi, Lattice defects formulated ferromagnetism in nonmagnetic La (III) ion doped NiO nanostructures: Role of oxygen vacancy. *Journal of Alloys and Compounds*. 825, 154071 (2020)
68. N. Madubuonu, S. O. Aisida, I. Ahmad, S. Botha, T. K. Zhao, M. Maaza, F. I. Ezema, Bio-inspired iron oxide nanoparticles using Psidium guajava aqueous extract for antibacterial activity. *Applied Physics A*, 126(1), 1-8 (2020)
69. J. Al Boukhari, A. Khalaf, R. S. Hassan, R. Awad, Structural, optical and magnetic properties of pure and rare earth-doped NiO nanoparticles. *Applied Physics A*. 126(5), 1-13 (2020)
70. H. Zhang, D. Zeng, Z. Liu, The law of approach to saturation in ferromagnets originating from the magnetocrystalline anisotropy. *Journal of magnetism and magnetic materials*. 322(16), 2375-2380 (2010)
71. A. J. Christy, S. Suresh, L. C. Nehru, Enhanced antibacterial and photocatalytic activities of nickel oxide nanostructures. *Optik*. 237, 166731 (2021)

72. S. Thambidurai, P. Gowthaman, M. Venkatachalam, S. Suresh, Enhanced bactericidal performance of nickel oxide-zinc oxide nanocomposites synthesized by facile chemical co-precipitation method. *Journal of Alloys and Compounds*. 830, 154642 (2020)
73. A. A. Ezhilarasi, J. J. Vijaya, K. Kaviyarasu, L. John Kennedy, R. Jothi Ramalingam, Hamad A. Al-Lohedan, Green synthesis of NiO nanoparticles using *Aegle marmelos* leaf extract for the evaluation of in-vitro cytotoxicity, antibacterial and photocatalytic properties. *Journal of Photochemistry and Photobiology B: Biology*. 180, 39-50 (2018)
74. P. Kumar, M. C. Mathpal, G. K. Inwati, S. Ghosh, V. Kumar, W. D. Roos, H. C. Swart, Optical and surface properties of Zn doped CdO nanorods and antimicrobial applications. *Colloids and Surfaces A: Physicochemical and Engineering Aspects*. 605, 125369 (2020)
75. A. A. Ezhilarasi, J. J. Vijaya, K. Kaviyarasu, X. Zhang, L. J. Kennedy, Green synthesis of nickel oxide nanoparticles using *Solanum trilobatum* extract for cytotoxicity, antibacterial and photocatalytic studies. *Surfaces and Interfaces*. 20, 100553 (2020)